WILEY-VCH

DOI: 10.1002/((adma.201902587))
Article type: Communication

Microwave Energy Drives "*on-off-on*" Spin-Switch Behavior in Nitrogen-Doped Graphene

Giorgio Zoppellaro,[,†,#] Aristides Bakandritsos,[†,#] Jiří Tuček,[†] Piotr Błoński,[†] Toma Susi,[‡] Petr Lazar,[†] Zdeněk Bad´ura,[†] Tomáš Steklý,[†] Ariana Opletalová,[†] Michal Otyepka,[†] and Radek Zbořil*[,†]*

†Regional Centre of Advanced Technologies and Materials, Department of Physical Chemistry, Faculty of Science, Palacký University Olomouc, Šlechtitelů 27, 783 71 Olomouc, Czech Republic

‡University of Vienna, Faculty of Physics, Boltzmanngasse 5, 1090 Vienna, Austria

E-mail: radek.zboril@upol.cz, zoppellarogiorgio@gmail.com

Keywords: Fluorographene, nitrogen doping, spin switch, spin-polarized states, spintronics

The established application of graphene in organic/inorganic spin-valve spintronic assemblies is as a spin transport channel for spin-polarized electrons injected from ferromagnetic substrates. To generate and control spin-injection without such substrates, the graphene backbone must be imprinted with spin-polarized states and itinerant-like spins. Computations suggest that such states should emerge in graphene derivatives incorporating pyridinic nitrogen. We report the synthesis and electronic properties of nitrogen-doped graphene (N content: 9.8%) featuring both localized spin centers and spin-containing sites with itinerant electron properties. This material exhibits spin-switch behavior (*on-off-on*) controlled by microwave irradiation at X-band frequency. This phenomenon may enable the creation of novel types of switches, filters, and spintronic devices using sp^2-only 2D systems.

Spintronics is a developing field of electronics that exploits both the charge and the spin of electrons to perform logic operations and to process, store, and transmit information.[1] Because spin-polarized currents encode more information than charge alone, a diverse spectrum of efficient spintronic logic, transmission, and storage devices have been envisaged, including spin-field-effect transistors, spin-light-emitting diodes, spin-resonant tunneling components, spin-modulators and encoders, and quantum bits. They are expected to have many advantages over traditional semiconductor-based alternatives, including higher data processing speeds, lower power consumption, non-volatility, and higher integration densities.[2] A central goal of spintronics is to identify materials exhibiting spin-dependent effects, which are required for the occurrence of spintronic processes.[1] Graphene was recently suggested to be an attractive platform for spintronic applications[3–5] because it exhibits several spin-related phenomena including tunnel magnetoresistance,[6] enhancement of spin injection efficiency,[7] the Rashba effect,[8] the quantum spin Hall effect,[9] and large perpendicular magnetic anisotropy.[10] It also exhibits several properties useful in spintronics, including ballistic charge transport,[11] long spin lifetimes and spin diffusion lengths,[12,13] limited hyperfine interactions,[14] gate-tunable magnetic order,[15] and weak spin-orbit coupling.[3] Due to its exceptionally long spin lifetime of ~10 ns (corresponding to a spin-diffusion length of several micrometers at room temperature), graphene has an intriguing spin-conserving potential. It is thus regarded as a promising material for spin transport in spin valve architectures, enabling faithful transmission of information encoded in a carrier's spin across a device.[4] However, because of its diamagnetism and weak spin-orbit coupling,[16] it exhibits only weak transport-current-induced spin densities and weakly spin-polarized currents. Pristine graphene cannot function as a spin-generator or an injector of spin-polarized carriers,[4] but strain induced in the material arising from surface corrugation and lattice mismatch between graphene layers and underlying substrates can severely change the electronic, magnetic and transport properties.[17,18] Strain effects are known to promote

modification of the graphene band gap and can induce spin gap asymmetry and spin polarization effects, locally or even extended over the 2D carbon network,[17,19] thus the "strain engineering" approach bears great potential for its application in graphene-based nano-fabrication technologies.[18,20] For example, Yan W. and co-authors have shown that cooperativity between strain and out-of-plane distortion in the graphene wrinkles provide valley-polarized sites with significant energy gaps, a property that offers the ground for realization of high-temperature *zero-field* quantum valley Hall effects.[21] Y. Liu *et al.*, upon interfacing graphene with orthorhombic black phosphorus (BP), demonstrated that both lattices can be mutually strained and sheared in such a way to create periodically fluctuating pseudo-magnetic fields (PMFs), and valley polarization could be manipulated by application of an external magnetic field, offering a route for developing a valley filter (valleytronics).[22] However, to create graphene spintronic devices without the underneath aid of inorganic ferromagnetic substrates, one must embed diverse spin-polarized domains directly into the graphene backbone. Spin valve behavior, which is fundamental to spintronics, requires the presence of two types of spin components (see **Figure 1**A): (i) localized spin centers (S_L) and (ii) spin-containing sites with itinerant electron properties (S_I). Furthermore, these spin-systems must interact within the molecular framework (J_{ex}).

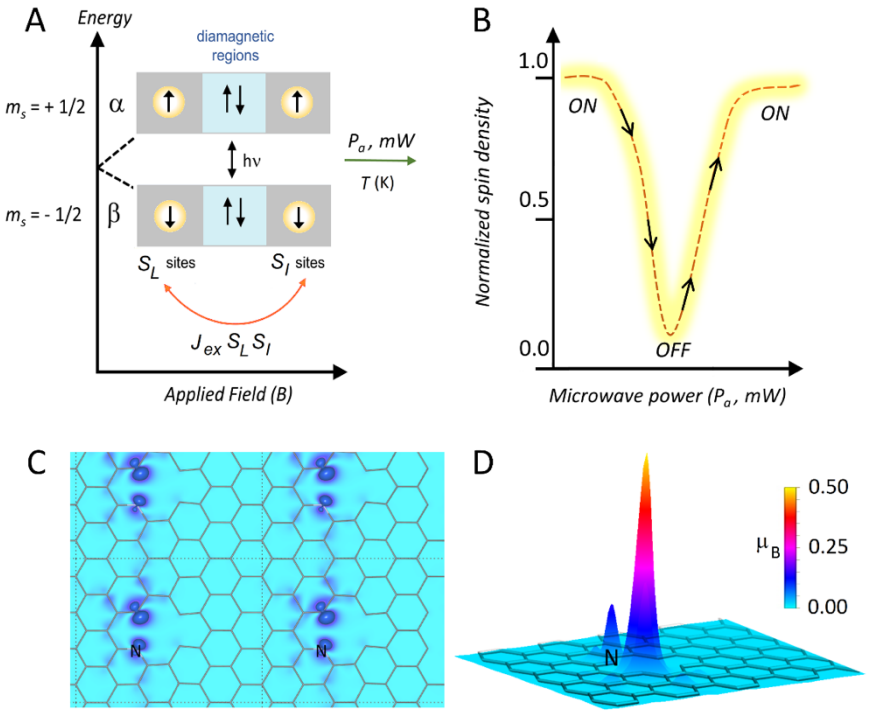

Figure 1. The spin-switch effect in pyridinic N-doped graphene is driven by the exchange interaction between two spin domains. a) Model of two distinct spin systems (the S_L and S_I sites) embedded in nitrogen-doped graphene, separated by a diamagnetic region, showing the effective spin polarization and transitions between the two electronic Zeeman levels (± ½) in an external magnetic field (B) with an appropriate phonon energy ($h\nu$). When the exchange interaction (J_{ex}) exceeds k_BT and under the application of large microwave flux density (P_a), spin flip-flop transitions from uncoupled and saturated S_I and S_L sites intercross the energy band of the coupled system (S_IS_L). b) This causes spin-injection of polarized electrons into the S_IS_L band. c) First-principles density functional theory calculations show the theoretical charge density distribution in the spin-up channel corresponding to the energy range between -0.5 eV and Fermi energy (E_F) in the density of states (DOS) plot shown in Figure 2D and Figures S2 and S3. The Vienna Ab-initio simulation package (VASP, cutoff energy of 600 eV) and the Perdew–Burke–Ernzerhof (PBE) approximation were used. The extent of the computational cell is indicated by the dashed lines. d) Calculated magnetic moment (in μ_B) distribution within the cell, corroborating the charge density distribution shown in panel (c).

A major challenge is to identify or create systems in which these spin components coexist and are spatially separated while maintaining an intimate electronic interaction. Several strategies for altering the electronic/magnetic and spin-related properties of graphene have been evaluated. These include doping/substitution of the graphene lattice with non-carbon atoms, adsorption of atoms, sp^3 functionalization, edge engineering and spatial confinement.[16] Functionalization is very effective at enhancing spin-orbit coupling, imprinting and stabilizing ferromagnetic or antiferromagnetic order at relatively high temperatures.[16,23–26] However, it introduces disorder and sp^3 defects that restrict charge mobility and reduce the spin relaxation length.[27,28] Theoretical studies indicate that while spatial confinement and edge engineering can induce the emergence of polarized spins and currents, this is most likely to occur in graphene nanoribbons below a threshold width, with a specific edge geometry[29–32] or edge functionalization (e.g. graphene nanoribbons functionalized with stable spin-bearing radical groups).[33] Therefore, despite its challenges,[34,35] doping with n- or p-type heteroatoms may be the most practical way to equip graphene with localized spins while maintaining a charge carrier concentration high enough to preserve its conductivity. In this context, nitrogen doping is envisioned as a method to imprint active centers into graphene to create materials suitable for organic-based spintronics.[36–40] Błoński *et al.*[36] recently reported that ferromagnetic spin ordering emerges in graphene doped with graphitic nitrogen. Conversely, Ito *et al.*[38] reported that pyrrolic nitrogen reduced the effective spin content of graphene and suppressed its magnetic response. However, the influence of pyridinic nitrogen on the evolution of magnetic features in graphene and its effects on potential spintronic behavior are unstudied. More importantly, due to the electron-donating nature and spin-inducing capability of nitrogen in graphene, 2D systems doped with pyridinic N could contain both spin-generating and spin-conserving regions and could thus operate in the spin-injection and spin-

transport regimes simultaneously, opening a route to advanced multifunctional spintronic materials.[4]

In this work we report a new graphene-based material containing extensive pyridinic N-doping that acts as spin-switch, in an "*on-off-on*" fashion, under microwave energy. Two spin systems with distinct natures (the S_L and S_I fractions) coexist within this material, as predicted by first-principles calculations (Figure 1C,D and Figures S1–S3). We observed that spin flip-flop processes arising from relaxation of the magnetic moments of the S_L and S_I fractions intercrossed the energy band associated with the exchange-coupled (J_{ex}) high-spin system, S_IS_L. Polarized spin transfer occurred below a threshold temperature (T) when the material was exposed to a sufficiently high microwave flux density (P_a), which caused a dramatic increase in the net spin polarization of the high-spin component. Pyridinic ^{14}N-doped graphene is thus a microwave energy-driven spin-switch material (Figure 1B), with intrinsic spin-dependent properties that arise from its chemical structure and can be manipulated at X-band frequency using microwaves. Electric and magnetic fields are commonly used to modulate spin injection in spin valve systems; our results demonstrate for the first time that microwave irradiation can be used for this purpose in graphene-based spin-valve architectures.

To produce graphene with a high content of pyridinic motifs, a system with high content of vacancies would be required. Preliminary studies in our lab established the formation of vacancies upon chemical treatment of fluorographene (FG), therefore we attempted to prepare highly pyridinic N-doped graphene (pNG) using the versatile chemistry of FG.[25,41–44] FG was reacted with hydroxylamine (NH_2OH) at 130 °C in dimethylformamide (DMF), avoiding high-temperature treatment or highly reactive reagents, used previously.[45,46,47] The Supporting Information presents a detailed characterization of pNG and the mechanism of its formation, which involves (i) the defluorination of FG and its transformation into highly N-doped (9.8 at. %) graphene (see Figure S4A–D), (ii) the

decomposition of hydroxylamine into ammonia, (identified by trapping the byproducts of the reaction, as described in Figure S4E), which undergoes dehydrogenation at vacancies[48–50] and is thus the source of the atomic nitrogen that becomes doped into the graphene lattice, (iii) the *in situ* formation of lattice vacancies in FG (see Figure S5A,B), and (iv) the formation of a predominantly sp^2 architecture (Figure S5C,D). Atomic force microscopy (AFM) and transmission electron microscopy (TEM) indicated that pNG consisted mainly of nanosized flakes (Figure 2A and Figure S6, respectively). Figures 2B and 2C show carbon and nitrogen elemental mappings of pNG flakes obtained by scanning transmission electron microscopy/energy-dispersive X-ray spectroscopy (STEM-EDS), revealing that the material exhibits very homogeneous N-doping (within the limit of the instrument resolution of a few nm). This was attributed to the well-defined stoichiometry of FG, which ensures that all carbon centers in the starting material are equally susceptible to transformation. As predicted by first-principles calculations (Figure 2D and Figures S1–S3), pyridinic nitrogen motifs enable the emergence of two interacting spin-populations: (i) a strong spin-up channel near the E_F, corresponding to ferromagnetically interacting localized spins (S_L) consisting predominantly of the in-plane p_{xy} orbitals of the undercoordinated carbons in divacancies (DV), and (ii) the valence band, which is dominated by delocalized Cp_z electrons (the S_I spin population) and overlaps with the S_L population, as shown in Figure 2D. In addition, small magnetic moments are present on carbon atoms near DV defects and between defects (Figure 1C,D), where the charge/spin densities are more dispersed (delocalized) along the σ-bonds. The system has a very small electron gap, which is on the order of several tens of meV and could be further reduced or even closed in the presence of graphitic nitrogen (as discussed below). Consequently, a relatively mild stimulus should be enough to induce the injection of spin-up electrons into the conduction band.

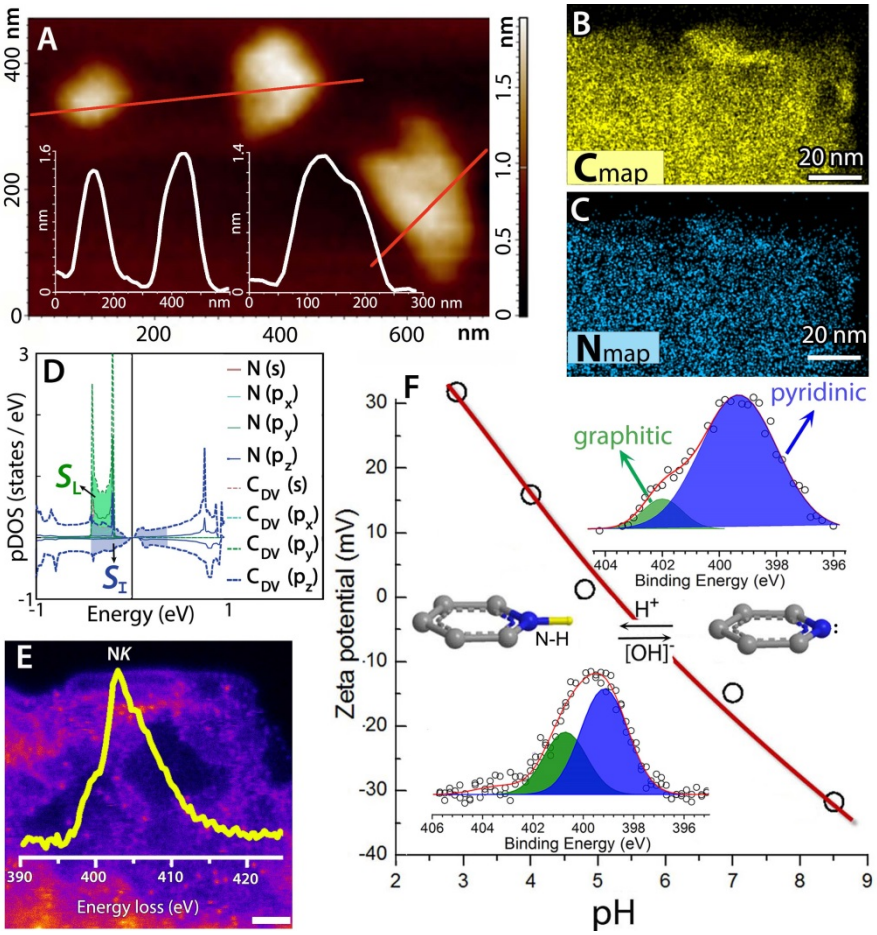

Figure 2. Characterization of pyridinic N-doped graphene (pNG). a) AFM image of pNG on mica support, showing single layer graphene nanoflakes. The insets show the flakes' height profiles. b–c) STEM-EDS elemental mapping of a pNG nanoflake for (b) carbon and (b) nitrogen. d) Orbital-resolved partial theoretical DOS of graphene doped with pyridinic N. C_{DV} denotes carbon atoms adjacent to a DV defect, and energies are quoted relative to E_F. e) STEM-MAADF image of a region near the edge of a pNG nanoflake and (overlay) the corresponding background-subtracted nitrogen electron energy loss spectrum. Scale bar: 1 nm (see also Figure S8). f) Apparent surface charge (*zeta potential*) of an aqueous pNG suspension as a function of pH. Insets show the deconvoluted N1s HR-XPS spectra of the protonated (left) and deprotonated (right) pNG.

The predominantly pyridinic character of the nitrogen dopants in pNG was verified experimentally using three independent techniques. First, scanning tunneling medium-angle annular dark-field (STEM-MAADF) and electron energy loss spectroscopy (EELS) analyses indicated that the background-subtracted N *K* response of pNG is consistent with pyridinic N (Figure 2E).[51] Second, the pH-dependence of the apparent surface charge (ζ_p, zeta potential) of a pNG suspension in water indicated that the material's point-of zero charge is ~5.3 (Figure 2F), coinciding with the pK_a of pyridine (5.2).[52] Third, the N1s HR-XPS spectrum of the partially protonated (as-prepared) pNG features two N components (Figure 2F, left spectrum): a low binding energy (BE) component attributed to pyridinic N and a high BE component that could be attributed to either pyrrolic N or protonated pyridinic N; N-protonation is known to increase BE.[53] Conversely, the N1s spectrum of pNG deprotonated by repeated alkaline washings (Figure 2F, right spectrum) could be fitted with a single symmetric Gaussian component with a BE typical for pyridinic N. In this case, a minor high BE (402 eV) component attributed to graphitic N was observed, which was reported to reduce further the band gap.[36] Finally, theoretical modeling of the IR spectra corroborated the assignment of the pyridinic configuration (Figure S7).

The predicted difference in the nature of the S_L and S_I spin-containing domains was verified experimentally by electron paramagnetic resonance spectroscopy (EPR) experiments using pNG samples doped with ^{14}N (p-^{14}NG) and samples isotopically enriched with ^{15}N (p-^{15}NG). EPR results unveiled the importance of the presence of nitrogen nuclear hyperfine fields (I_N) for the emergence of the "*on-off-on*" spin-switch behavior. Specifically, the EPR spectrum of p-^{14}NG (T = 118 K, 0.3 mW, Figure 3A, i) is consistent with an organic-based radical, featuring a sharp Lorentzian-type derivative signal (ΔB_{pp} = 13.0 Gauss, Figure S10A) centered at a g_{eff} of 1.997. This signal is complemented by broad wings that develop asymmetrically in the low and high field regions. The overall signal could not be simulated using perturbation theory in the spin-Hamiltonian framework by a single S = 1/2 transition,

whether of Gaussian, Lorentzian, or Voigt-shape type. Instead, the resonance appears to be a superposition of (i) a narrow Lorentzian-component (Figure 3A, i; simulated in Figure S10A with isotropic *g*-tensor of 1.997) and (ii) a broad Gaussian component with an anisotropic *g*-tensor (g_1 of 2.060, $g_{2,3}$ of 1.997, and g_{eff} = 2.018, red line in Figure 3A, i). The Lorentzian component is related to localized unpaired electrons (S_L) that experience strong exchange regime, resulting in a narrow signal, negligible zero-field-splitting, and no appreciable interaction with the ^{14}N atoms (and thus do not give rise to any hyperfine term in the Hamiltonian expression, $\hat{H} = \beta_e g \hat{S} B_0 - \Sigma_n 2J\hat{S}_L\hat{S}_{L-1}$. The broad signal is associated in p-^{14}NG to itinerant S = 1/2 electrons. Here, the hyperfine terms with nearby ^{14}N nuclei are active but remain poorly resolved and are thus responsible for the observed resonance field broadening ($\hat{H} = \beta_e g \hat{S}_I B_0 - \Sigma_n 2J\hat{S}_I\hat{S}_{I-1} + \Sigma_n \hat{S}_I A_N I_N$). Because of these nuclear hyperfine interactions, the spin-spin relaxation time calculated for the Gaussian component was appreciably shorter (T_2 ~0.4×10^{-9} s) than that for the non-interacting Lorentzian component (T_2 ~0.5×10^{-8} s). To confirm the presence of the N-hyperfine field interactions, we recorded the EPR spectrum of p-^{15}NG, whose hyperfine interactions differ from those of p-^{14}NG because the nuclear spin of ^{15}N is I = 1/2 whereas that of ^{14}N is I = 1. Two distinct spin components were also observed in the p-^{15}NG spectrum: one Lorentzian (simulated in Figure S10B) and one Gaussian (red line in Figure 3B, i). However, a simulation of the broad component in the spin-Hamiltonian framework using second-order perturbation theory (Figure 3B, red trace, g_1 of 2.009, $g_{2,3}$ of 1.997, and g_{eff} = 2.001) predicted it to have weaker signal asymmetry and a smaller resonance-field spread (ΔB of 500 G for p-^{15}NG *vs* ΔB of 700 G for p-^{14}NG) than the corresponding component in the p-^{14}NG spectrum. These results are in harmony with the weaker hyperfine field associated to ^{15}N nuclei (I = 1/2). The presence of stronger hyperfine interactions in the p-^{14}NG system for the generation and control of an "*on-off-on*" spin-switch behavior became apparent upon recording the EPR signals of p-^{14}NG (Figure 3A, ii) and

p-^{15}NG (Figure 3B, ii) at higher microwave power levels (P_a = 120 mW). The entire resonance spectrum of p-^{15}NG exhibited only a slight symmetric broadening at high P_a, without indication of significant shift in g_{eff}; this indicates a small energy spread (ΔE) associated to the ground <↓> and excited <↑> energy levels of the two spin configurations in both domains, S_I and S_L. In contrast to an isolated atom where unpaired electrons can interact only with one nucleus, the electrons confined in pNG can interact with several N lattice nuclei with different strength (through Fermi contact and dipolar couplings), similarly as being immersed in a bath of nuclear spins.[54] The hyperfine spin-Hamiltonian ($\hat{H} = \Sigma_n \hat{S}_I A_N I_N$) for S_I can be viewed, in the simplest scenario with uniform hyperfine couplings, as a Heisenberg type spin function. The isotropic hyperfine interaction for electrons in an s-type conduction band in which the Fermi contact part dominates has been described as $\hat{H} = \Sigma_n \hat{S}_I A_N I_N = \hat{S} \times \boldsymbol{h}$, with $\boldsymbol{h} = \Sigma_n A_N I_N$ and A =4/3 ($\mu_0 g_I \mu_N \mu_B |u_0|^2$) with u_0 being the Bloch function amplitude. For *s*-type conduction band electrons, the effective magnetic field $\boldsymbol{h}$ induced by nuclei onto the electron spin moment is referred to as the Overhauser field.[55] Small distribution in $\boldsymbol{h}$ produces narrow Overhauser fields and decreases the so-called electron spin decoherence effect induced by hyperfine terms, which is the decay of phase information encoded in the electron spin.[56] We hypothesize that in p-^{15}NG there exists only a small quantum admixture of the S_I and S_L wavefunctions, the distribution in Overhauser field ($\boldsymbol{h}$) is small for S_I, and the S_I and S_L magnetic relaxation regimes are weakly perturbed by their mutual presence in the lattice, as can be seen later in the power-saturation experiments. On the contrary, for p-^{14}NG, the entire resonance signal exhibits an extreme broadening at high P_a and at 118 K (*i.e.*, a very pronounced increase in the magnetic field spread, ΔB, which reached ~1750 G) being accompanied by clear shift in *g*-value (g_{eff} ~ 2.030). This phenomenon suggests a larger energy spread of the pertinent S_I states (large $\boldsymbol{h}$ spread) owing to the large perturbation of the electron-spin moments by stronger anisotropic fields from the ^{14}N-nuclear hyperfine

components (I = 1). Additional EPR spectra are given in the Supporting Information (EPR traces for p-^{14}NG in Figures S11–S14 and for p-^{15}NG in Figures S15–S17).

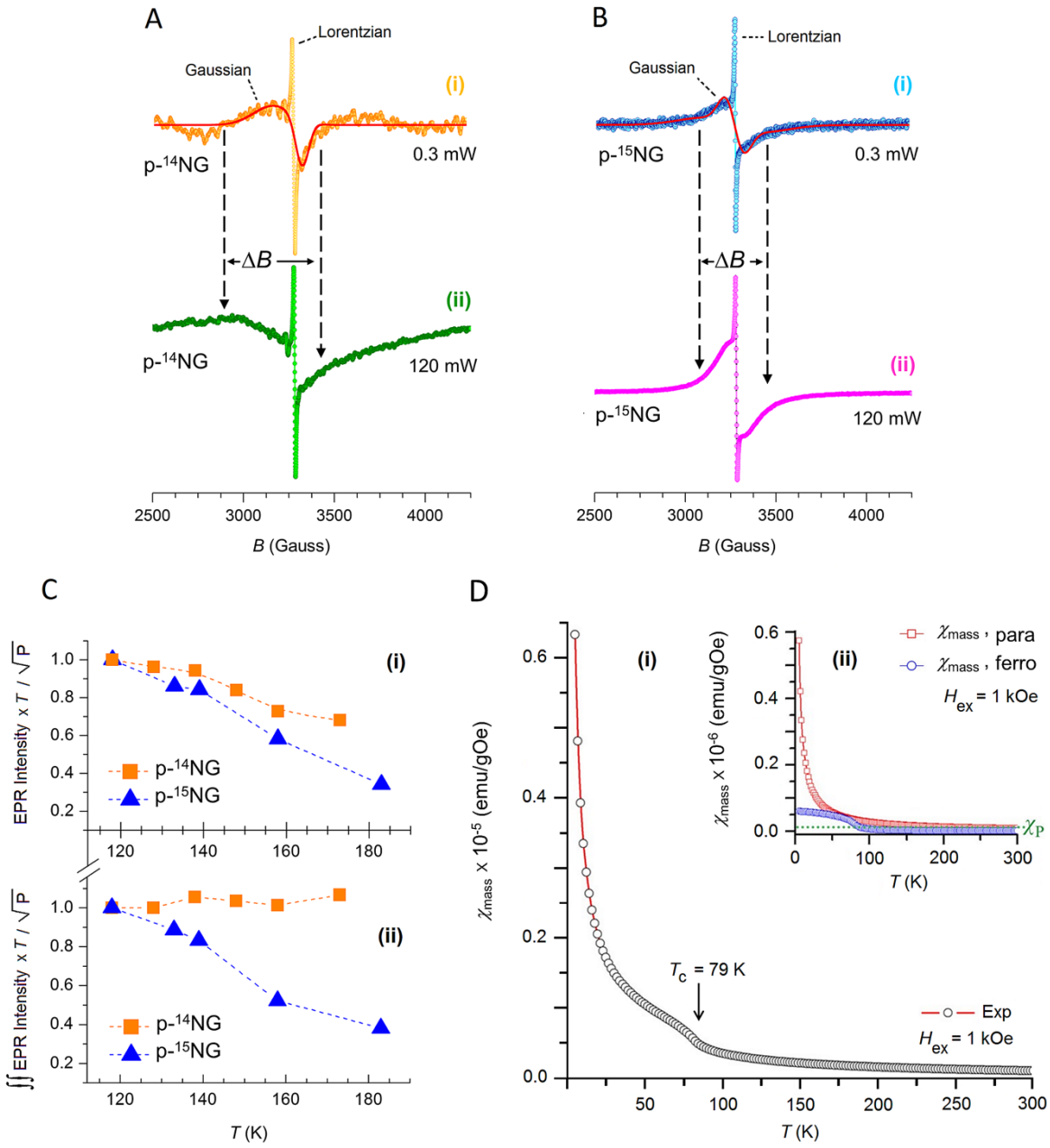

Figure 3. The two types of spin domains in pNG materials and their magnetic behavior revealed by EPR and bulk susceptibility. X-band (9.1-9.2 GHz, 100 kHz modulation frequency) EPR spectra of the N-doped graphene materials recorded at T = 118 K. a) p-^{14}NG recorded at 0.3 mW (i) and 120 mW (ii), and b) p-^{15}NG recorded at 0.3 mW (i) and 120 mW (ii). All samples were analyzed in a freshly dispersed frozen matrix of DMF. The red lines

show the results of simulations of the broad component (S_I) using the parameters specified in the text. c) Temperature dependence of the spin concentration in p-^{14}NG (square) and p-^{15}NG (triangle) for (i) the Lorentzian component alone (intensity-based: $I_{EPR} \times T/\sqrt{P}$ *vs* T) and (ii) the Gaussian (S_I) and Lorentzian (S_L) components combined (total area-based, $\iint I_{EPR} \times T/\sqrt{P}$ *vs* T). d) (i) Mass magnetic susceptibility, χ_{mass}, vs T of p-^{14}NG, measured under and external magnetic field of 1 kOe. (ii) Mass magnetic susceptibility for paramagnetic, $\chi_{mass,para}$, and ferromagnetic, $\chi_{mass,ferro}$, fraction as a function of temperature.

Analysis of the variation of the spin concentration in p-^{14}NG and p-^{15}NG *vs* temperature (see Figure 3C and Figures S18 and S19) gives further insight of the temperature-dependent behavior associated to the S_I and S_L spin domains. For the Lorentzian component (S_L), the temperature dependence of the EPR intensity-based spin-concentration departed from Curie behavior in both systems, p-^{14}NG (experimental data: squares, Figure 3C, i) and p-^{15}NG (experimental data: triangles, Figure 3C, i), which is indicative of the strong exchange regime ($J_{ex1}S_L \cdot S_L$) with ferromagnetic interactions ($I_{EPR} \times T/\sqrt{P} \neq C$, with C being the Curie constant). However, the temperature dependence of the total EPR signal area-based spin-concentration (which is dominated by the broad S_I component rather than the narrow S_L one) revealed clear differences between p-^{14}NG and for p-^{15}NG (Figure 3C, ii). The p-^{15}NG system keeps the ferromagnetic behavior (Figure 3C ii, triangles) and both S_L and S_I domains exhibit ferromagnetic character. Here the exchange interaction (J_{ex1}) for the $S_L \cdot S_L$ domains and (J_{ex2}) for the $S_I \cdot S_I$ domains dominate over the cross-exchange term ($J_{ex1,2}$) $S_I \cdot S_L$, in agreement with the proposed small quantum admixture of the S_I and S_L spin-wavefunctions. The p-^{14}NG system, on the contrary, followed a Curie-trend (Figure 3C ii, squares). The latter result suggests that in p-^{14}NG the S_I systems are perturbed more substantially by large anisotropic hyperfine fields, hence the cross-exchange term ($J_{ex1,2}$) associated to the $S_I \cdot S_L$ spin

configuration dominates; in particular, besides the ferromagnetic (S_L) domain seen in the sharp Lorentzian component, the S_I domain shows a dominant Pauli-type (temperature-independent) behavior. This effect must originate from a more efficient quantum admixture of the S_I domains with part of the S_L sites in p-^{14}NG, forming S_I-S_L, a Fermi-degenerate two-dimensional electron system. Electronic fingerprints of this type are typical of conducting electrons with Pauli character (Fermi-degenerate electron systems).[57] The presence of such electrons is consistent with our theoretical calculations, which correlated the S_I spin population with the valence band derived primarily from the delocalized Cp_z (and Np_z) electrons (Figure 2D). The coexistence of distinct spin systems in p-^{14}NG was also confirmed by recording the temperature dependence of the mass magnetic susceptibility (χ_{mass}) (Figure 3D) and its hysteresis loop at 5 K (Figure S20). In accordance with the EPR data, two magnetically diverse regions were identified, with overlapped contribution; one characterized by significant magnetic interactions that promote ferromagnetic ordering at low temperature (~79 K), and a second domain, exhibiting temperature-independent contribution (in the degenerate limit) from conduction (itinerant) electrons. The latter behavior was fully consistent with the conduction-electron fraction responsible for the Gaussian component observed in the EPR spectra. To investigate further the different magnetic behavior of p-^{14}NG and p-^{15}NG at high microwave power, we studied the total area-based spin concentrations (Figure 4A) upon increasing the applied microwave energy flux, P_a (*i.e.*, their saturation behavior).

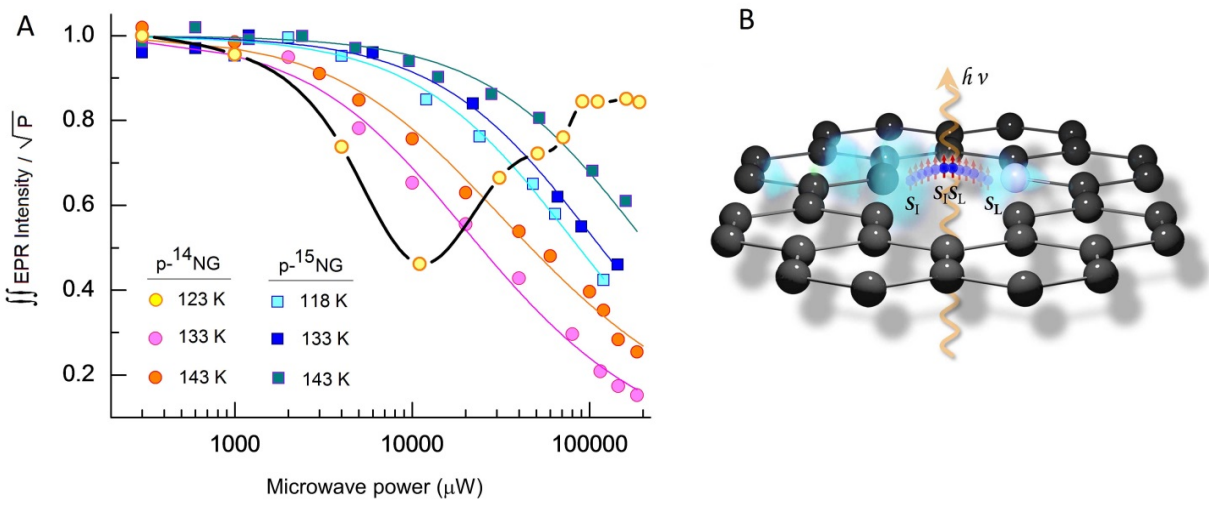

Figure 4. The microwave induced spin-switch effect in pNG. a) EPR power saturation plot showing the emergence of the spin-switch phenomenon in p-^{14}NG (experimental data, circles) at low temperature (123 K) compared to its normal saturation behavior expressed at higher temperatures (133 K and 143 K). The saturation trend of p-^{15}NG (experimental data, squares), on the contrary, follows at all probed temperatures (118 K, 133 K and 143 K) the saturation behavior expected from the theory. The plots are based on analysis of the EPR spectra considering the entire resonance line ($\iint I_{EPR}/\sqrt{P}$), normalized against the maximum observed intensity. The solid lines in the data-plots result from fitting analysis of the data according to the Portis and Castner's theory. The black line for p-^{14}NG at 123 K is given here as guide to the eye. b) Schematic representation of the population of the $S_L S_I$ band with spin-polarized electrons upon increasing the applied microwave power.

For p-^{15}NG, the net spin-concentration decreased substantially as P_a increased which was well described by Portis and Castner's theory[58,59] (Equation (1) in the Supporting Information). Fitting based on this theory (see the solid lines in Figure 4A) indicated that the spin-packets associated with the S_I and S_L components are not cross-correlated, *i.e.*, the sharp and broad components of Figure 3B behave as independent (non-correlated) spin domains.

The fitting analysis yielded the following estimated values at 143 K ($P_{1/2}$ = 158.7 mW, b = 1.6), at 133 K ($P_{1/2}$ = 84.6 mW, b = 1.6), and at 118 K ($P_{1/2}$ = 63.2 mW, b = 1.6). As expected, the half-saturation value ($P_{1/2}$) decreases upon lowering the temperature, in full agreement with the theory. The value obtained for the shape factor b is also consistent with the analysis of the EPR resonance envelopes, characterized by an admixture of Gaussian and Lorentzian lines, and further validates the conclusion that the S_I and S_L spin components are magnetically uncorrelated (*i.e.*, when spin systems exhibit $b > 1$).[60,61] The recorded evolution of the power saturation EPR traces in p-^{15}NG, obtained at 118 K, 133 K, and at 143 K, are given in the Supporting Information (Figures S21–S23). The power saturation behavior of p-^{14}NG was, indeed, very different from that expressed by p-^{15}NG (Figure 4A). At high temperature (at 143 K and at 133 K) the EPR resonance lines saturate much faster than those observed for p-^{15}NG, giving, from fitting analysis, the following values of $P_{1/2}$ = 15.5 mW, b = 1.0 at 143 K, and $P_{1/2}$ = 13.2 mW, b = 1.33 at 133 K. At 123 K the saturation behavior of p-^{14}NG could not be analyzed in the framework of the Portis and Castner's theory. At this temperature, the spin population in p-^{14}NG decreased sharply until the applied microwave power reached 11 mW, at which point it increased sharply before plateauing when the microwave power reached 91 mW. This behavior is unprecedented and suggests the occurrence of an "*on-off-on*" transfer of polarized spins, thus interpreted in terms of spin-switch effects (see Figures S24–S26 for the power saturation EPR traces of p-^{14}NG at 123 K, 133 K, and 143 K). The phenomenon was explained by proposing that the new exchange-coupled high-spin state ($S_I S_L$) is populated (beyond its normal Boltzmann distribution) when T is sufficiently low and J_{ex} exceeds the available thermal energy ($k_B T \leq$ 123 K). These interactions are reminiscent of those seen in metals and semiconductors, where the conduction electrons (the S_I in this case) are bound to localized spins (the S_L in this case) via an exchange energy interaction (J_{ex}).[62,63] In p-^{14}NG, flip-flop transitions may connect the power-saturated S_I and S_L states with the new unsaturated

$S_I S_L$ coupled state, transferring local field energy away from the saturated states and resulting in polarized spin injection when P_a exceeds a certain threshold. This dynamic process of feeding $S_I S_L$ then plateaus at ~91 mW (Figure 4A), at which point P_a and dP_a/dB become proportional to H_1^2 (eq. (7) in the Supporting Information), and the thermodynamic process of relaxation occurs again in accordance with the Portis and Castner's saturation theory. Because this phenomenon is not observed in p-^{15}NG, the exchange interaction ($J_{ex1,2} S_I S_L$) must be mediated by the anisotropic $AI_N S$ terms (originating from the interactions with the strong p-^{14}N nuclear hyperfine fields), which are key for the through-bond propagation of spin-polarization and quantum admixture of the S_I and S_L states.

These experimental results were in full agreement with the theory-based prediction that graphene doped with pyridinic N would contain two spin populations on p_{xy} and p_z orbitals that overlap in energy, with the latter extending very close to and above the Fermi level (the S_L and S_I populations, respectively). The experimental observation of multiple strong p-^{14}NG nuclear hyperfine interactions with the p_z spins should be considered responsible for the wide energy distribution of the p_z DOS in the DFT calculations. These features, along with the very small band gap in DOS, enable the S_L-S_I interaction and the injection of spin polarized electrons (given a sufficient microwave flux density) to an energy level lying extremely close to the conduction band (the coupled S_I-S_L state), generating a microwave-controlled spin-switch, as illustrated in Figure 4B. From the analysis of the (three) as-synthesized batches of the p-^{14}NG material, we observed that while the spin-switch behavior was clearly expressed at the same temperature threshold (123 K) in all cases, the power-dependent switching effect became active (in one batch) under microwave irradiation flux, P_a, as low as 4 mW at T = 123 K, (see Supporting material, Figures S27-S28). This observation indicates that the hyperfine-dependent switching phenomenon is dictated by the subtle combination of the mutual distance (R) and angles (θ) between the spin domains S_I and

S_L belonging to the different sublattices, $J_{ex1,2(SI\cdot SL)} \propto 1/R^3$ and $J_{ex1,2(SI\cdot SL)}(\mathbf{R}) \propto \sin^2(\theta)_{SI\cdot SL}$,[64] as well as by the effective number (N) of interacting S_I and S_L sites involved in the cross-exchange process (ΔN population of the coupled state modulate the spin-lattice relaxation term, T_1, and in turn dictates changes in P_a, see Equations 2, 6 and 7 in the Supporting material). This is clearly one of the limits of the "wet-chemistry" synthetic methodology, because the exact positioning in the lattice of the doping nitrogens (and spin containing S_L sites) cannot be achieved with atomic precision.

The results presented in this work pave the way to sp^2-only 2D systems exhibiting spin-switch behavior induced at X-band frequencies by microwave energy. . The possible doping of graphene with other elements e.g phosphorous[65,66] (^{31}P, I = ½, natural abundance 100%, nuclear magnetic moment μ_I/μ_N of 1.1316) or arsenic (^{75}As, I = 3/2, natural abundance 100%, nuclear magnetic moment μ_I/μ_N of 1.4395),[67] which encode nuclear hyperfine fields of different strengths, may offer further possibilities for investigating the impact of hyperfine interactions and application of microwave energy on the emergence of spin switch behavior in organic materials. Controlled spin switch behavior (ON-OFF) and transport properties are the current focus of research in several laboratories (in academy and industry) for devising a new generation ofgraphene-based transistors. These materials and devices have shown some promise, as well as several limitations, for future development in semiconductor electronics, for digital logic and radiofrequency devices [68,69]. Carbon nanotubes in fact have been explored as potential building blocks for signal routing in future microwave networks,[70] and in high-frequency signal processing applications,[71] while graphene layers have been shown to be more suitable for building RF devices with high cutoff frequencies (acting as frequency filters).[72,73] Therefore, the results presented here may stimulate further research into the alternative generation and control of spin-polarized electron injection in graphene-based materials, enabling the potential assembly of a novel class of spintronic and FET devices.

Corresponding Authors

*E-mail: radek.zboril@upol.cz, Phone: +420 585634337, Fax: +420 585634761 (R.Z.)

*E-mail: zoppellarogiorgio@gmail.com, Phone: +420 585634950, Fax: +420 585634958 (G.Z.)

Author Contributions

G.Z. performed EPR experiments and analysis thereof, Z.B assisted on the EPR experiment execution. A.B. synthesized the pNG material, performed IR, zeta potential, XPS, Raman and TGA-MS analysis. J.T. performed analysis of bulk susceptibility measurements. T. Steklý contributed in synthesis of various batches of the materials and collected IR and zeta-potential data. A.O. performed AFM and Raman measurements. T. Susi performed STEM-MAADF and EELS measurements and analysis. P.B. performed the theoretical calculations and analysis. P.L. performed the theoretical IR calculations. M.O. contributed with fruitful suggestions and comments on the design of theoretical calculations and their interpretation. G.Z., A.B., J.T., and R.Z. wrote the manuscript. [#]G.Z. and A.B. contributed equally.

Supporting Information. Detailed synthesis of the nitrogen-doped graphene (pNG), structural and physicochemical characterization data including FT-IR spectra, Raman spectra, details and discussion on electrokinetic measurements, XPS analysis, TGA-MS analysis, TEM and EELS analysis, STEM-MAADF analysis, bulk magnetic susceptibility (PPMS) analysis, additional EPR spectra and computational data and analysis. Supporting Information is available from the Wiley Online Library or from the authors.

Acknowledgements

The authors gratefully acknowledge support from the Operational Programme Research, Development and Education – European Regional Development Fund, Project No. CZ.02.1.01/0.0/0.0/16_019/0000754 of the Ministry of Education, Youth, and Sports of the Czech Republic and the assistance provided by the NanoEnviCz Research Infrastructure supported by the Ministry of Education, Youth and Sports of the Czech Republic under Project No. LM2015073. P. B. acknowledges institutional support from the Palacký University in Olomouc, Czech Republic. T. S. acknowledges the Austrian Science Fund (FWF) project P 28322-N36 and the European Research Council (ERC) Grant (H2020) No. 756277-ATMEN. M. O. acknowledges funding from an ERC Consolidator Grant (H2020) No. 683024. The authors thank Ms. Jana Stráská, Mr. Ondřej Tomanec, Dr. Ondřej Malina, Dr. Martin Petr and Dr. Juri Ugolotti (all from the Regional Centre of Advanced Technologies and Materials, Faculty of Science, Palacký University Olomouc, Czech Republic) for TEM, HR-TEM/STEM-EDS, magnetization, XPS and TGA-MS measurements, respectively. Mrs Šárka Adámková is acknowledged for the synthesis of a third batch of the p-^{14}NG material.

Conflict of Interest

The authors declare no competing financial interest.

References

[1] I. Žutić, J. Fabian, S. Das Sarma, *Rev. Mod. Phys.* **2004**, *76* (2), 323–410.

[2] S. A. Wolf, D. D. Awschalom, R. A. Buhrman, J. M. Daughton, S. von Molnár, M. L. Roukes, A. Y. Chtchelkanova, D. M. Treger, *Science* **2001**, *294* (5546), 1488–1495.

[3] W. Han, R. K. Kawakami, M. Gmitra, J. Fabian, *Nat. Nanotechnol.* **2014**, *9*, 794–807.

[4] D. Pesin, A. H. MacDonald, *Nat. Mater.* **2012**, *11*, 409–416.

[5] S. Roche, J. Åkerman, B. Beschoten, J. -C. Charlier, M. Chshiev, S. Prasad Dash, B. Dlubak, J. Fabian, A. Fert, M. Guimarães, F. Guinea, I. Grigorieva, C. Schönenberger, P. Seneor, C. Stampfer, S. O. Valenzuela, X. Waintal, B. van Wees, *2D Mater*. **2015**, *2* (3), 030202.

[6] E. Cobas, A. L. Friedman, O. M. J. van't Erve, J. T. Robinson, B. T. Jonker, *Nano Lett*. **2012**, *12* (6), 3000–3004.

[7] W. Han, K. Pi, K. M. McCreary, Y. Li, J. J. I. Wong, A. G. Swartz, R. Kawakami, *Phys. Rev. Lett*. **2010**, *105*, 167202.

[8] Y. S. Dedkov, M. Fonin, U. Rüdiger, C. Laubschat, *Phys. Rev. Lett*. **2008**, *100*, 107602.

[9] C. L. Kane, E. L. Mele, *Phys. Rev. Lett*. **2005**, *95*, 226801.

[10] H. Yang, A. Duc Vu, A. Hallal, N. Rougemaille, J. Coraux, G. Chen, A. K. Schmid, M. Chshiev, *Nano Lett*. **2016**, *16* (1), 145–151.

[11] A. S. Mayorov, R. V. Gorbachev, S. V. Morozov, L. Britnell, R. Jalil, L. A. Ponomarenko, P. Blake, K. S. Novoselov, K. Watanabe, T. Taniguchi, A. K. Geim, *Nano Lett*. **2011**, *11* (6), 2396–2399.

[12] T.-Y.Yang; J. Balakrishnan, F. Volmer, A. Avsar, M. Jaiswal, J. Samm, S. R. Ali, A. Pachoud, M. Zeng, M. Popinciuc, G. Güntherodt, B. Beschoten, B. Özyilmaz, B. *Phys. Rev. Lett*. **2011**, *107*, 047206.

[13] B. Dlubak, M.-B. Martin, C. Deranlot, B. Servet, S. Xavier, R. Mattana, M. Sprinkle, C. Berger, W. A. De Heer, F. Petroff, A. Anane, P. Seneor, A. Fert, *Nat. Phys*. **2012**, *8*, 557–561.

[14] C. Cervetti, A. Rettori, M. G. Pini, A. Cornia, A. Repollés, F. Luis, M. Dressel, S. Rauschenbach, K. Kern, M. Burghard, L. Bogani, L. *Nat. Mater.* **2016**, *15*, 164–168.

[15] D. A. Abanin, P. A. Lee, L. S. Levitov, *Phys. Rev. Lett.* **2006**, *96*, 176803.

[16] J. Tuček, P. Błoński, J. Ugolotti, A. K. Swain, T. Enoki, R. Zbořil, *Chem. Soc. Rev.* **2018**, *47* (11), 3899–3990.

[17] S. Nigar, Z. Zhou, H. Wang, M. Imtiaz, *RSC Advances* **2017**, *7*, 51546-51580.

[18] N.-C. Yeh, C.-C. Hsu, M. L. Teague, J.-Q. Wang, D. A. Boyd, C.-C. Chen, *Acta Mech. Sin.* **2016**, *32*, 497-509.

[19] F. Guinea, M. I. Katsnelson, A. K. Geim, *Nat. Phys.* **2010**, *6*, 30-33.

[20] C. Si, Z. Sun, F. Liu, *Nanoscale*, **2016**, *8*, 3207-3217.

[21] W. Yan, W.-Y. He, Z.-D. Chu, M. Liu, L. Meng, R.-F. Dou, Y. Zhang, Z. Liu, J.-C. Nie, L. He, *Nat. Commun.* **2013**, *4*, 2159.

[22] Y. Liu, J. N. B. Rodrigues, Y. Z. Luo, L. Li, A. Carvalho, M. Yang, E. Laksono, J. Lu, Y. Bao, H. Xu, S. J. R. Tan, Z. Qiu, C. H. Sow, Y. P. Feng, A. H. C. Neto, S. Adam, J. Lu, K. P. Loh, *Nature Nanotechnology* **2018,** *13*, 828–834.

[23] R. R. Nair, M. Sepioni, I. -L.Tsai, O. Lehtinen, J. Keinonen, A. V. Krasheninnikov, T. Thomson, A. K. Geim, I. V. Grigorieva, *Nat. Phys.* **2012**, *8*, 199–202.

[24] J. Tuček, P. Błoński, Z. Sofer, P. Šimek, M. Petr, M. Pumera, M. Otyepka, R. Zbořil, *Adv. Mater.* **2016**, *28* (25), 5045–5053.

[25] J. Tuček, K. Holá, A. B. Bourlinos, P. Błoński, A. Bakandritsos, J. Ugolotti, M. Dubecký, F. Karlický, V. Ranc, K. Čépe, M. Otyepka, R. Zbořil, *Nat. Commun.* **2017**, *8*, 14525.

[26] A. Avsar, J. Y. Tan, T. Taychatanapat, J. Balakrishnan, G. K.W. Koon, Y. Yeo, J. Lahiri, A. Carvalho, A. S. Rodin, E. C. T. O'Farrell, G. Eda, A. H. Castro Neto, B. Özyilmaz, *Nat. Commun.* **2014**, *5*, 4875.

[27] M. Wojtaszek, I. J. Vera-Marun, T. Maassen, B. J. van Wees, *Phys. Rev. B* **2013**, *87*, 081402(R).

[28] J. Balakrishnan, G. Kok Wai Koon, M. Jaiswal, A. H. Castro Neto, B. Özyilmaz, *Nat. Phys.* **2013**, *9*, 284–287.

[29] Y. -W. Son, M. L. Cohen, S. G. Louie, *Nature* **2006**, *444*, 347–349.

[30] O. Hod, V. Barone, J. E. Peralta, G. E. Scuseria, *Nano Lett.* **2007**, *7* (8), 2295–2299.

[31] E. -j. Kan, Z. Li, J. Yang, J. G. Hou, *J. Am. Chem. Soc.* **2008**, *130* (13), 4224–4225.

[32] Y. Li, Z. Zhou, P. Shen, Z. Chen, *ACS Nano* **2009**, *3* (7), 1952–1958.

[33] M. Slota, A. Keerthi, W. K. Myers, E. Tretyakov, M. Baumgarten, A. Ardavan, H. Sadeghi, C. J. Lambert, A. Narita, K. Müllen, L. Bogani, *Nature* **2018**, *557*, 691–695

[34] C. N. R. Rao, K. Gopalakrishnan, A. Govindaraj, *Nano Today* **2014**, *9* (3), 324–343.

[35] U. N. Maiti, J. Lim, K. E. Lee, W. J. Lee, S. O. Kim, *Adv. Mater.* **2014**, *26* (4), 615–619.

[36] P. Błoński, J. Tuček, Z. Sofer, V. Mazánek, M. Petr, M. Pumera, M. Otyepka, R. Zbořil, *J. Am. Chem. Soc.* **2017**, *139*, 3171–3180.

[37] Q. Miao, L. Wang, Z. Liu, B. Wei, F. Xu, W. Fei, *Sci. Rep.* **2016**, *6*, 21832.

[38] Y. Ito, C. Christodoulou, M. V. Nardi, N. Koch, M. Kläui, H. Sachdev, K. Müllen, *J. Am. Chem. Soc.* **2015**, *137* (24), 7678–7685.

[39] A. P. Alegaonkar, A. Kumar, S. H. Patil, K. R. Patil, S. K. Pardeshi, P. S. Alegaonkar, *J. Phys. Chem. C* **2013**, *117* (51), 27105–27113.

[40] A. L. Friedman, C. D. Cress, S. W. Schmucker, J. T. Robinson, O. M. J. van't Erve, *Phys. Rev. B* **2016**, *93*, 161409(R).

[41] A. Bakandritsos, M. Pykal, P. Błoński, P. Jakubec, D. D. Chronopoulos, K. Poláková, V. Georgakilas, K. Čépe, O. Tomanec, V. Ranc, A. B. Bourlinos, R. Zbořil, M. Otyepka, *ACS Nano* **2017**, *11* (3), 2982–2991.

[42] D. D. Chronopoulos, A. Bakandritsos, P. Lazar, M. Pykal, K. Čépe, R. Zbořil, M. Otyepka, *Chem. Mater.* **2017**, *29* (3), 926–930.

[43] P. Lazar, C. K. Chua, K. Holá, R. Zbořil, M. Otyepka, M. Pumera, *Small* **2015**, *11* (31), 3790–3796.

[44] R. Zbořil, F. Karlický, A. B. Bourlinos, T. A. Steriotis, A. K. Stubos, V. Georgakilas, K. Šafářová, D. Jančík, C. Trapalis, M. Otyepka, *Small* **2010**, *6* (24), 2885–2891.

[45] D. Guo, R. Shibuya, C.Akiba, S. Saji, T. Kondo, J. Nakamura, S*cience* **2016**, *351* (6271), 361–365.

[46] J. Song, Z. Yu, M. L. Gordin, D. Wang, *Nano Lett.* **2016**, *16* (2), 864–870.

[47] D. Deng, X. Pan, L. Yu, Y. Cui, Y. Jiang, J.; Qi, W. -X. Li, Q. Fu, X. Ma, Q. Xue, G. Sun, X. Bao, *Chem. Mater.* **2011**, *23* (5), 1188–1193.

[48] X.-F. Li, K.-Y. Lian, L. Liu, Y. Wu, Q. Qiu, J. Jiang, M. Deng, Y. Luo, *Sci. Rep.* **2016**, *6*, 23495.

[49] R. A. Bueno, J. I. Martínez, R. F. Luccas, N. R. del Árbol, C. Munuera, I. Palacio, F. J. Palomares, K. Lauwaet, S. Thakur, J. M. Baranowski, W. Strupinski, M. F. López, F. Mompean, M. García-Hernández, J. A. Martín-Gago, *Nat. Commun.* **2017**, *8*, 15306.

[50] B. Wang, L. Tsetseris, S. T. Pantelides, *J. Mater. Chem. A* **2013**, *1*, 14927–14934.

[51] Y. -C. Lin, P. -Y. Teng, C. -H. Yeh, M. Koshino, P. -W. Chiu, K. Suenaga, *Nano Lett.* **2015**, *15* (11), 7408–7413.

[52] H. Kiuchi, R. Shibuya, T. Kondo, J. Nakamura, H. Niwa, J. Miyawaki, M. Kawai, M. Oshima, Y. Harada, *Nanoscale Res. Lett.* **2016**, *11*, 127.

[53] D. Nolting, E. F. Aziz, N. Ottosson, M. Faubel, I. V. Hertel, B. Winter, *J. Am. Chem. Soc.* **2007**, *129* (45), 14068–14073.

[54] M. Fuchs, V. Rychkov, B. Trauzettel, *Phys. Rev. B* **2012**, *86*, 085301.

[55] J. Schliemann, A. Khaetskii, D. Loss. *Journal of Physics: Cond. Matt.* **2003**, *15*, R1809.

[56] J. Jing, L.-A. Wu, *Sci. Rep.* **2018**, *8*, 1471.

[57] N. Fujita, D. Matsumoto, Y. Sakurai, K. Kawahara, H. Ago, T. Takenobu, K. Marumoto, *Sci. Rep.* **2016**, *6*, 34966.

[58] T. J. Jr. Castner, *Phys. Rev.* **1959**, *115* (6), 1506–1515.

[59] A. M. Portis, *Phys. Rev.* **1953**, *91* (5), 1071–1078.

[60] G. Zoppellaro, A. Geies, K. K. Andersson, V. Enkelmann, M. Baumgarten, *Eur. J. Org. Chem.* **2008**, *8*, 1431–1440.

[61] G. Zoppellaro, A. Geies, V. Enkelmann, M. Baumgarten, *Org. Lett.* **2004**, *6* (26), 4929-4932.

[62] J. Winter, *Magnetic Resonance in Metals*. Clarendon Press, Oxford, 1971.

[63] D. J. Lépine, *Phys. Rev. B* **1970**, *2* (7), 2429–2439.

[64] M. Agarwal and E. G. Mishchenko, *Phys. Rev. B* **2019**, *99*, 085439.

[65] P. A. Denis, Chem. Phys. Lett. 2010, 492, 251-257.

[66] a) A. R. MacIntosh, G. Jiang, P. Zamani, Z. Song, A. Riese, K. J. Harris, X. Fu, Z. Chen, X. Sun, G. R. Goward, *J. Phys. Chem. C* **2018,** *122*, 6593-6601; b) T. Susi, T. P Hardcastle, H. Hofsäss, A. Mittelberger, T. J Pennycook, C. Mangler, R. Drummond-Brydson, A. J Scott, J. C Meyer, J. Kotakoski, *2D Materials* **2017**, *4* (2), 021013.

[67] P.A. Denis, *ChemPhysChem* **2014**, *15* (18), 3994-4000.

[68] C. Rutherglen, D. Jain, P. Burke, *Nat. Nanotech.* **2009**, 4 (11), 811–819.

[69] F. Schwierz, *Nat. Nanotech.* **2010**, *5*, 487-496.

[70] S. Li, Z. Yu, S.-F. Yen, W. C. Tang, P. J. Burke, *Nano Lett.* **2004**, *4***,** 753–756.

[71] G. De Angelis, A Lucibello, E Proietti, R Marcelli, D. Pochesci, G. Bartolucci, M. Dragoman, D. Dragoman, *Nanomater. nanotechnol.* **201**1, 1 (1), 64-77.

[72] G. Deligeorgis, M. Dragoman, D. Neculoiu, D. Dragoman, G. Konstantinidis, A. Cismaru, R. Plana, *App. Phys. Lett.* **2009**, *95*, 073107.

[73] M. Dragoman, D. Neculoiu, D. Dragoman, G. Deligeorgis, G. Konstantinidis, A. Cismaru, F. Coccetti, R. Plana, *IEEE Microwave Magazine* **2010**, *11* (7), 81-86.

The "*on-off-on*" spin-switch process, which involves spin-polarized unpaired electrons, emerges in nitrogen doped graphene material. The spin-switch phenomenon is activated below a temperature threshold and upon application of high microwave energy density fluxes.

Keyword: Fluorographene, nitrogen doping, spin switch, spin-polarized states, spintronics

Giorgio Zoppellaro,* Aristides Bakandritsos, Jiří Tuček, Piotr Błoński, Toma Susi, Petr Lazar, *Zdeněk Bad'ura*, Tomáš Steklý, Ariana Opletalová, Michal Otyepka and Radek Zbořil*

Microwave Energy Drives "*on-off-on*" Spin-Switch Behavior in Nitrogen-Doped Graphene

TOC

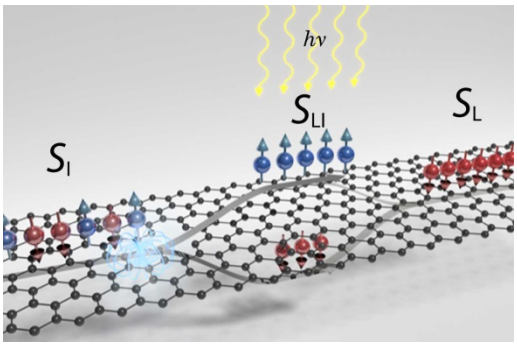

Supporting Information

Microwave Energy Drives "*on-off-on*" Spin-Switch Behavior in Nitrogen-Doped Graphene

Giorgio Zoppellaro,[,†,#] Aristides Bakandritsos,[†,#] Jiří Tuček,[†] Piotr Błoński,[†] Toma Susi,[‡] Petr Lazar,[†] Zdeněk Bad´ura,[†] Tomáš Steklý,[†] Ariana Opletalová,[†] Michal Otyepka,[†] and Radek Zbořil*[,†]*

[†]Regional Centre of Advanced Technologies and Materials, Department of Physical Chemistry, Faculty of Science, Palacký University Olomouc, Šlechtitelů 27, 783 71 Olomouc, Czech Republic

[‡]University of Vienna, Faculty of Physics, Boltzmanngasse 5, 1090 Vienna, Austria

Number of figures: 28

Materials and methods

Reagents and materials. Graphite fluoride (>61 wt. % F, $C_1F_{1.1}$), hydroxylamine hydrochloride (^{14}N, 99%), sodium hydroxide, hydrochloric acid, ACS reagent, 37%, dimethyl sulfoxide (DMSO, p.a), acetone p.a., dichloromethane (DCM, p.a.), and ethanol, p.a were purchased from Sigma-Aldrich. Hydroxylamine hydrochloride (^{15}N, 98%) was purchased from Santa Cruz Biotechnology. Acetone (pure), ethanol (absolute), amine-free dimethylformamide (DMF), and nitric acid (Analpure®, 65%) were obtained from Lach-ner. All aqueous solutions were prepared with ultrapure water (18 MΩ cm^{-1}).

Synthesis of the nitrogen-doped graphene (pNG). Fluorinated graphite (200 mg, ~6.5 mmol of CF units) was added in a 50 mL round-bottom glass flask and degassed three times by vacuum and backfiling with nitrogen. Then, 15 mL of DMF was added in the flask and the mixture was degassed again for three times. It was left stirring at R.T. under nitrogen atmosphere for 24 h, before applying sonication for 4 h (under nitrogen) in a Bandelin Sonorex system (DT 255H type, frequency 35 kHz, power 640 W, effective power 160 W). Then 450 mg of NH_2OH•HCl (~6.5 mmol) was added in the flask and degassed for three times. Sonication was applied in order to exfoliate the fluorinated graphite. The mixture was heated at 130 °C with a condenser under stirring (350 rpm). Sample aliquots were withdrawn from the spherical flask at different time intervals in order to monitor the course of the reaction. Intermediates and final product, at 30 h of reaction, were left to cool down to room temperature. The materials were separated by centrifugation and further purified by successive washing steps using DMF (3×), DMSO (2×), DCM (2×), acetone (2×), ethanol (2×), acidified water (2×, pH = 2), and ultrapure water (4×). Hot DMF and water were also applied. During the last washing, the material was suspended in water and dispersed well by mixing and sonication, prior to centrifugation (500 rcf, 2 min). The supernatant was collected in order to obtain the fine fraction of the flakes. After this step, the material was suspended either in absolute ethanol, or water depending on the following characterization and reaction procedures. Three batches were in total synthesized and subjected to EPR measurements; in all the three batches similar spin-switch behavior were observed.

The same procedure was followed for the case of the ^{15}N-labelled hydroxylamine, to obtain the p-^{15}NG, with no nuclei containing hyperfine magnetic field, as in the case of ^{14}N-containing hydroxylamine.

Structural and physicochemical characterization

FT-IR spectra were recorded on an iS5 FTIR spectrometer (Thermo Nicolet) using the Smart Orbit ZnSe ATR accessory. Briefly, a droplet of an ethanolic dispersion of the relevant material was placed on the ZnSe crystal and left to form a film. Spectra were then acquired by summing 52 scans or more, using nitrogen gas flow through the ATR accessory. ATR and baseline corrections were applied to the collected spectra.

Raman spectra were recorded on a DXR Raman microscope using the 532 nm excitation line of a diode laser.

X-ray photoelectron spectroscopy (XPS) was carried out with a PHI VersaProbe II (Physical Electronics) spectrometer using an Al K_α source (15 kV, 50 W). The obtained data were evaluated and deconvoluted with the MultiPak (Ulvac - PHI, Inc.) software package. Spectral analysis included a Shirley background subtraction and peak deconvolution employing mixed Gaussian–Lorentzian functions.

Electron microscopy images were obtained with TEM JEOL 2010 with LaB_6 type emission gun, operating at 160 kV. STEM-HAADF (high-angle annular dark-field imaging) analyses for EDS (Energy-dispersive X-ray spectroscopy) mapping of elemental distributions on the products were performed with a FEI Titan HRTEM microscope operating at 80 kV. High-resolution images were recorded using an aberration-corrected Nion UltraSTEM100 instrument operated at 60 kV in near-ultrahigh vacuum using the MAADF (medium-angle annular dark-field) detector with an angular range of 80–200 mrad. Chemical analysis was further conducted via EELS (electron energy loss spectroscopy)[1], with an energy spread of approximately 0.35 eV and a dispersion of 0.47 eV px^{-1} for the C *K* survey and 0.24 eV px^{-1} for the N *K* fine structure spectra. For these analyses, a droplet of an aqueous dispersion of the material under study with a concentration of ~0.1 mg mL^{-1} was deposited on a carbon-coated copper grid and slowly dried at laboratory temperature for 24 hours to reduce its content of adsorbed water.

Thermal analyses were performed with an STA449 C Jupiter–Netzsch instrument at a heating rate of 5 °C min^{-1}, under an N_2 flow in the sample compartment. The masses of

released gases in the range of 12–60 *m/z* were determined with a QMS 403 Aëolos instrument (Netzsch), starting at 100 °C to avoid overloading the spectrometer with adsorbed water.

Electrokinetic measurements for the determination of the particles' mobility and zeta-potential (ζ_p) values were performed with a Malvern ZetaSizer Nano instrument.

Contact profilometer images were obtained on Taylor Hobson Ltd, Form Talysurf Series 2 at room temperature.

A physical property measurement system (PPMS, Quantum Design, U.S.A.) equipped with a vibrating sample magnetometer (VSM) was employed for collecting magnetization data of the sample. The temperature dependence of the sample's magnetization was measured upon warming in the temperature interval 2 to 300 K with a sweep rate of 1 K min^{-1} under an external magnetic field of 1 kOe after cooling in a field of 1 kOe. The sample's hysteresis loop was recorded in an external magnetic field ranging from –50 to 50 kOe and at a temperature of 5 K. Prior to analysis, the magnetization values were corrected by considering the response of the sample holder, sample capsule, and respective Pascal constants.

AFM measurements: The topography and phase image of pNG were obtained on an NTegra Prima with a HA-NC probe (Moscow) in the semicontact mode by depositing a drop of freshly dispersed material (water suspension, 1 mg mL^{-1}) on mica.

EPR measurements: EPR spectra were recorded on JEOL JES-X-320 operating at X-band frequency (9.17 GHz), equipped with a variable temperature control ES 13060DVT5 apparatus, and were performed on frozen solution (pNG suspended in DMF) samples. The cavity *Q* quality factor was kept above 6000 in all measurements. Highly pure quartz tubes were employed (Suprasil, Wilmad, ≤ 0.5 OD).

Estimation of the spin-spin relaxation time (T_2) was obtained using the relation $T_2 = 1/\gamma\Delta B_L = 2/\gamma\lambda_L\sqrt{3}$ (Refs. 2,3), where γ represents the gyromagnetic ratio (1.760859 10^{-7} s^{-1} $Gauss^{-1}$) and λ_L the peak-to-peak width of the derivative absorption line.

The spin populations in function of the temperature (presented in Figure 3C and Figures S18 and S19) are expressed in terms of signal intensity times temperature (Figure 3C i, $I_{EPR} \times T/\sqrt{P}$) and as double-integrated signal intensity of the entire resonance line times temperature

vs temperature (Figure 3C ii, $\iint I_{EPR} \times T/\sqrt{P}$ *vs* T). Values have been divided by the root of applied powers and normalized to the higher numerical value for easier comparison.

First-derivative EPR spectra were recorded at different microwave power (P) and at various temperatures to determine the microwave power at half saturation ($P_{1/2}$) for the examined temperature. Experimental data were treated using the following Equation (1), *i.e.*,

$$\iint S = k \times \sqrt{P}/[1 + (P/P_{1/2})]^{b/2}. \quad (1)$$

The term $\iint S$ corresponds to the double-integrated signal intensity (S), P is the applied microwave power, b is the relaxation factor (b = 1 for inhomogeneous line broadening, namely Gaussian type and b = 3 for homogeneous line broadening, namely Lorentzian type), $P_{1/2}$ is the power at which the signal is being half-saturated, and k is an experimental constant associated to the instrument. To apply Equation (1) the following experimental conditions must be satisfied: (i) the samples should be in a region of the cavity with maximum microwave field (H_1), thus the filling factor needs optimization, (ii) the sample temperature must be constant, and (iii) the frequency and the gain must also be kept constant. Equation (1), however, is not strictly applicable when dipolar couplings and/or exchange interactions are effective in the system. The half-saturation power ($P_{1/2}$) is defined by Equations (2) and (3), where V represents the cavity volume, Q the cavity quality factor ($Q = H_1^2V/2P$), P the power dissipated in the cavity, and γ the gyromagnetic ratio. Equation (2) assumes that all spins at resonance saturate equivalently, henceforth feature the same product ($T_1 \times T_2$).

$$P_{1/2} = \alpha/T_1 \times T_2, \quad (2)$$

$$\alpha = ½\ V/Q\gamma^2 \quad (3)$$

When dipolar and/or exchange interactions are present in the spin system, the product ($T_1 \times T_2$) is not constant, thus $1 \leq b \leq 3$ is no longer valid, and b becomes <1. Saturation of the EPR resonance line can be understood in terms of transition probabilities between spin population in the upper ($Z\uparrow$, α) and lower ($Z\downarrow$, β) energy levels, through Equations (4) and (5)

$$(Z\uparrow) = B_{lu}\rho_v + W(\uparrow), \quad (4)$$

$$(Z\downarrow) = A_{ul} + B_{lu}\rho_v + W(\downarrow), \quad (5)$$

where ρ_v represents the radiation density at frequency v to which the spin system is being exposed, $W(\uparrow)$ and $W(\downarrow)$ are the up and down transition probabilities per unit time, A_{ul} is the Einstein coefficient for spontaneous emission, B_{ul} and B_{lu} are the Einstein coefficients for stimulated emission and absorptions. Defining the spin population difference as $\Delta N = N_l - N_u$, *i.e.*, ΣS_n lower – ΣS_n upper, and the steady case $d\Delta N/dt = 0$ as ΔN^{ss}, it can be seen that:

$$\Delta N^{ss} = N\{[A_{ul} + W(\downarrow) - W(\uparrow)]/[A_{ul} + 2B_{ul}\rho_v + W(\downarrow) + W(\uparrow)]\} \quad (6)$$

Hence, when the radiation density ρ_v dominates in $(Z\uparrow)$ and $(Z\downarrow)$, then $\Delta N \rightarrow \Delta N^{ss} \rightarrow 0$ and there is no net absorption of the radiation by the spin system.

The rate at which the microwave energy per time unit (P_a) is adsorbed from the linearly polarized excitation field is given by Equation (7), *i.e.*,

$$P_a = \omega\{\omega_0^2\gamma_e^2(h/4\pi)\Delta N) \times \pi g(\omega-\omega_0)\}/[1 + \tfrac{1}{4}\pi\gamma_e^2H_1^2T_1g(\omega-\omega_0)], \quad (7)$$

where H_1 is the maximum amplitude of the microwave magnetic field, $\Delta N = N_l - N_u$ the spin population difference, and $g(\omega-\omega_0)$ the normalized shape factor for the spin transition. Increasing the microwave power produces spin transitions at a faster rate, thus decreases the spin-orientation lifetime, resulting in signal broadening up to the point that no resonance signal is observed.

Computational details. Electronic and magnetic properties of N-doped graphene have been studied by using first principles density functional code (Vienna Ab-initio simulation package, VASP code,[4] which employs plane-wave basis set; (here the cutoff energy was set to 600 eV) and projected augmented wave potentials (PAW)[5,6] to represent atomic cores. Electronic exchange and correlation effects were treated by using the Perdew, Burke, and Ernzerhof (PBE) generalized-gradient approximation (GGA).[7] The Brillouin zone was sampled using a 6 × 6 × 1 Γ-centered *k*-point mesh per conventional 4 × 3 rectangular cell and Gaussian smearing of 0.02 eV. The electronic density of states (DOS) was calculated using the tetrahedron method[8] with a 21 × 21 × 1 *k*-point mesh. Local magnetic moments were calculated by projecting the plane-wave components of all the occupied eigenstates onto spherical waves inside atomic spheres and integrating resulting local DOS.

Supplementary text and figures

Comments on theoretical results. The effect of both pyridinic and pyrrolic nitrogen atoms neighboring to the divacancy (DV) defect on the structural, electronic, and magnetic properties of graphene was studied. Up to four N atoms in the former configurations were considered corresponding to the experimental structure reported in Ref. 9. The pyrrolic nitrogen was initially placed inside the octagonal ring of the DV defect (see Figure S1). All the structures were optimized with a stringent relaxation criterion, 10 meV $Å^{-1}$ for the residual atomic forces and 10^{-6} eV for the electronic structure convergence. The initially pyrrolic N transformed into non-magnetic pyridinic N upon structural relaxation, as depicted in Figure S1. Figure S2 displays the density of states (DOS) diagram of graphene doped with pyridinic N (see also Figure 1C, main text) revealing a strong localized feature near the Fermi level (E_F) in the spin-up channel, which corresponds to the ferromagnetically interacting localized charge/spin densities and is predominantly composed of in-plane $p_{x,y}$ orbitals of undercoordinated C in the divacancy (C_{DV}). The valence band of Np_z electrons overlaps with this peak, which together with a rather tiny electron gap in the order of several tens of meV (which can be further reduced or even closed due to the graphitic nitrogen) can assist the injection of spin-up electrons to the conduction band. Due to the fact that multiple pyridinic N atoms tend to aggregate in the vicinity of defects (carbon vacancies), and in this sense they may be clustered (Ref. 9 and references there in), DOS calculations were also performed with two or three nitrogen atoms positioned at the divacancy (see Figure S3), which afforded the same conclusions regarding the spin distribution.

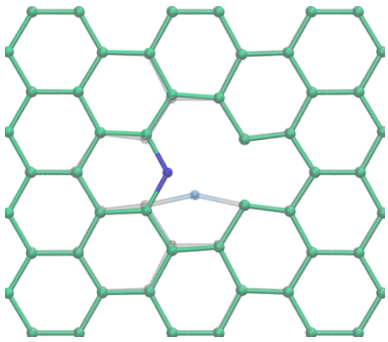

Figure S1. Stability of pyridinic nitrogen over pyrrolic. A single pyrrolic nitrogen (light blue) in graphene inside the octagonal ring of the DV defect. Structural optimization transforms pyrrolic N into pyridinic (dark blue). The initial and final graphene structure is shown respectively in gray and green.

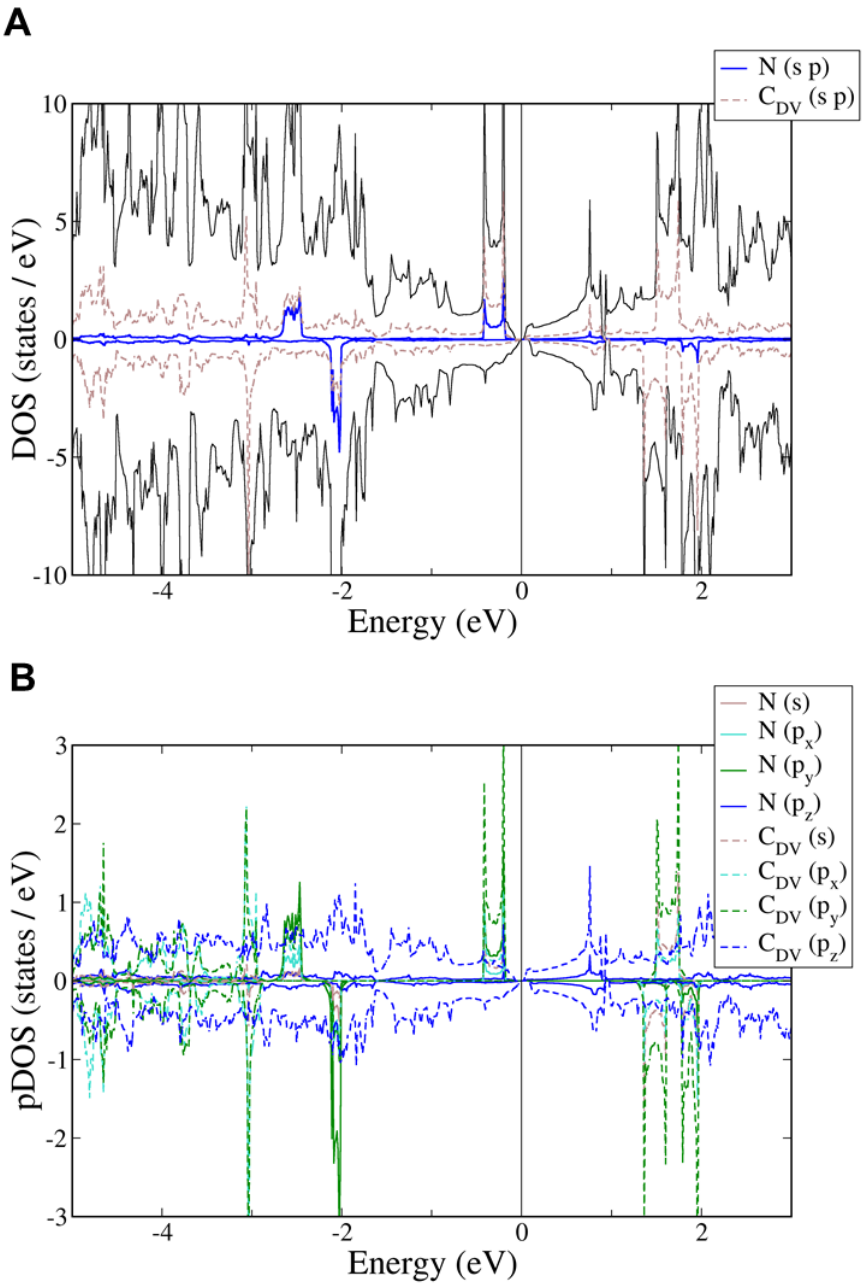

Figure S2. Theoretical density of states of graphene doped with pyridinic N (see also Figure 1C,D in the main text). **a)** Total (black line) and atom-resolved DOS and **b)** the corresponding orbital resolved partial DOS. C_{DV} stands for the carbon atoms neighboring to the DV defect. Energies are zeroed to E_F.

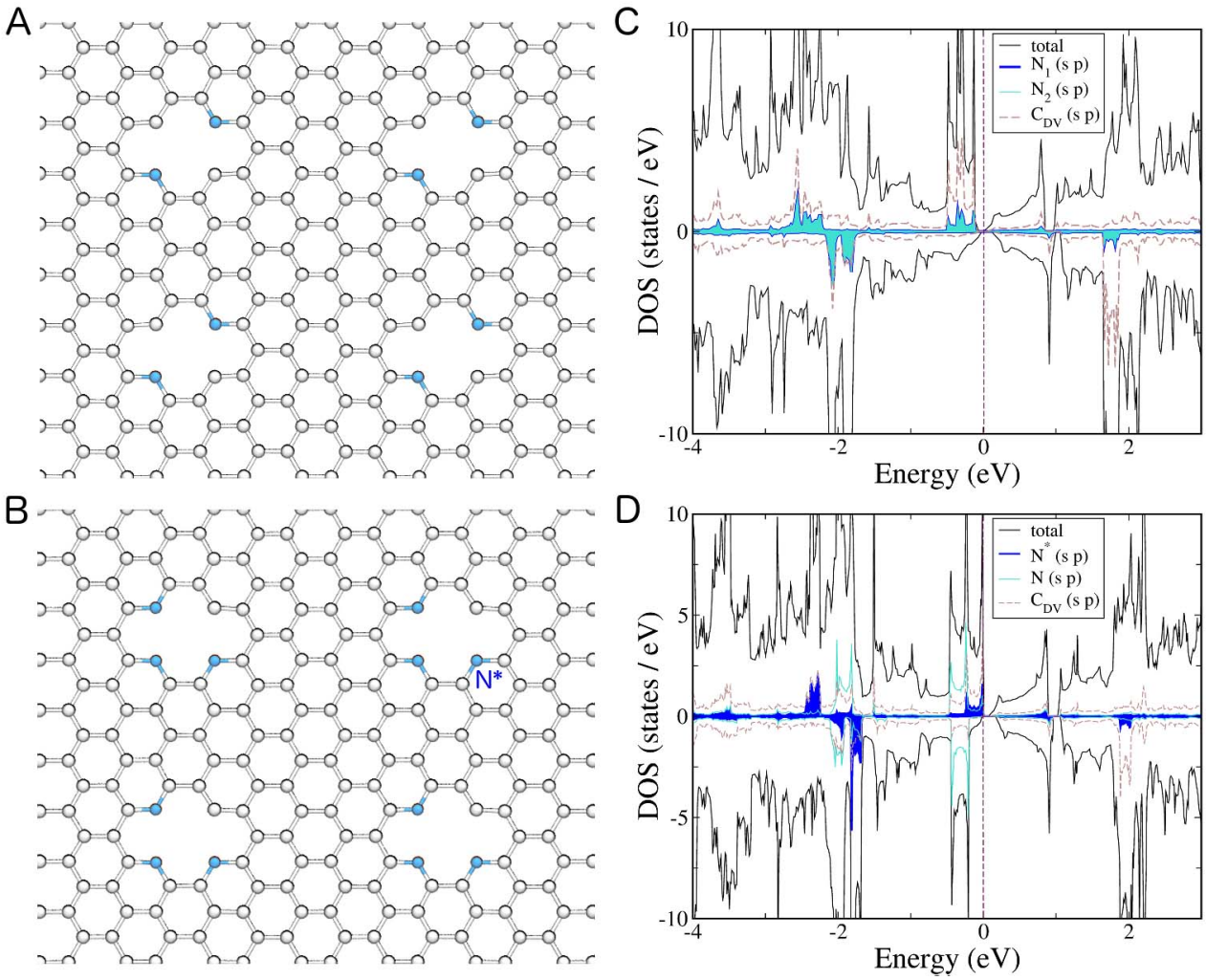

Figure S3. Theoretical density of states of graphene doped with pyridinic N. a) The case of two and **b)** three pyridinic nitrogens in a divacancy, with (C and D) the corresponding total and atom-resolved DOS. C_{DV} stands for the carbon atoms neighboring to the DV defect. Energies are zeroed to E_F.

Supporting results and analysis on the characterization of pNG material. Pyridinic nitrogen-doped graphene (pNG) was prepared by the reaction of fluorographene (FG) with NH_2OH•HCl·in DMF for 30 h, whereby defluorination and increasing N content progressively transformed FG from a very hydrophobic into a hydrophilic material, as indicated by the decreasing contact angles of water droplets (see Figure S4A). This was in full agreement with the elemental analysis from high-resolution X-ray photoelectron spectroscopy (HR-XPS) (see Figure S4B,C), showing significant defluorination (F content dropped to 7.7 from the 55 at. % originally present in pristine FG[10]. The N content in pNG reached 9.8 at. % with respect to the carbon atoms (8.6 % with respect to the total atoms in the system). The infrared spectra (see Figure S4D) also clearly showed that the C–F band at 1202 cm^{-1} was progressively reduced and a new band evolved at 1580 cm^{-1}, attributed to aromatic ring stretching vibrations,[11,12] since reductive defluorination in FG leads to restoration of the double bonds.[13,14] Additional vibrational modes of the aromatic rings appeared at 1500–1400 cm^{-1} (evident by the shoulders in the 30 h sample), and ascribed to heteroatom-substituted heterocyclic aromatic systems (such as in pyridinic configurations).[11,15] The lack of N–H vibrations above 3000 cm^{-1} implied low concentration or absence of $–NH_2$ and pyrrolic groups in the sample,[16] as also verified by theoretical calculations of the IR spectra for N-doped graphenes (see Figure S7). In pristine and defect-free graphene the ring stretching vibrations are IR inactive[17,18] because of the high symmetry of the system. Nevertheless, in presence of sp^3 defects or heteroatoms and vacancies the degeneracy is lifted. The spectrum of FG after 1 h reaction is still dominated by the covalent C-F bond vibrations in the spectral area from 1310 to 1110 cm^{-1} (see Figure S4D), being identical with that of pristine FG,[10,19] with maximum intensity centered at 1202 cm^{-1}. After 20 h of reaction, the C-F bonds are still evident, but have significantly decreased in intensity. This decrease allowed the observation of a band at 1110 cm^{-1}, probably preexisting and ascribed to semi-ionic C···F bonds.[20–23] In these bonds, the C···F distance is larger and thus lower electrophilicity and higher sp^2 character of the pertinent carbons is expected.[24,25] The less electrophilic character of these carbons is also verified by their lower ionization energy, as determined by XPS (*i.e.*, lower binding energy of the respective component, see Figure S5C and Ref. 26). Therefore, it is possible that these bonds are affected less from the changes triggered by the attack from the nucleophile species.

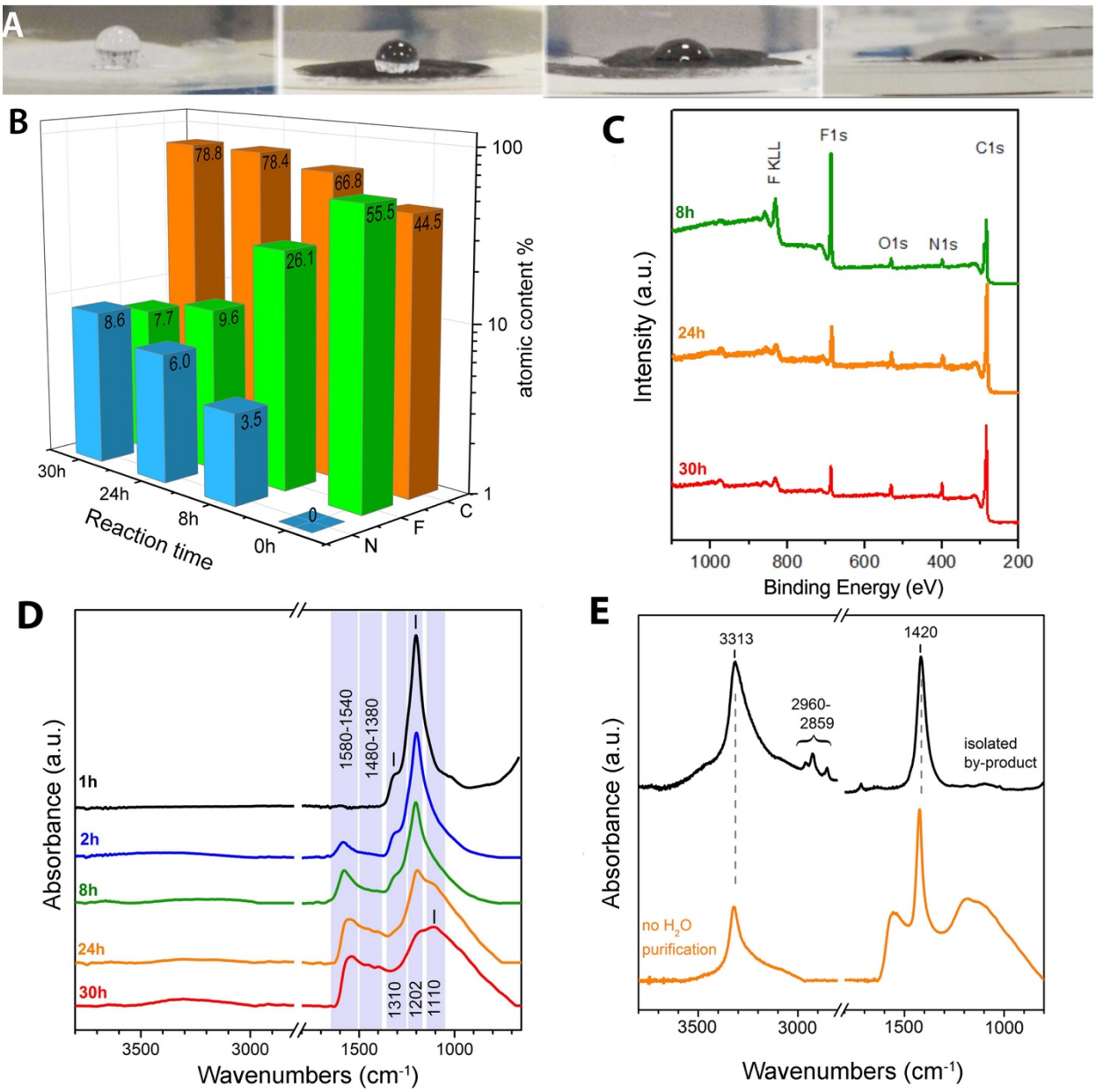

Figure S4. Structural characterization of the nitrogen-doped graphene. a) Contact angles of water droplets deposited on films made from the products of the reaction at different time points (0, 8, 24, and 30 h). **b)** HR-XPS-based elemental analysis, (C) XPS survey spectra, and **d)** FT-IR spectra of pNG and intermediates at different time points of the reaction. **e)** IR spectra of: (bottom spectrum) the product before purification with water, with IR bands from both pNG (as indicated in panel D, 30 h spectrum) and the NH_4F by-product; (upper spectrum) the by-product after its isolation from the aqueous-washings phase.

The high nitrogen content in pNG was ascribed to the reaction of FG with NH_3, which was released by the decomposition of NH_2OH during the reaction. Proof for the release of NH_3 was obtained after isolation of a by-product: before washing pNG with water, its IR spectrum revealed bands at 3313 and 1420 cm^{-1} (see Figure S4E), which were ascribed to NH_4F. NH_4^+ indeed displays these two characteristic IR vibrations[27] and the spectrum is identical with that reported for NH_4F, recorded after treatment of Si surfaces with NH_4F (Ref. 28). NH_4F is soluble only in water, thus explaining its detection in the product before water washing. These findings verify that during the reaction, NH_2OH is decomposed to NH_3 and in turn, NH_3 traps the released F^- ions from FG in the form of NH_4F. NH_4^+ may be formed by protonation of ammonia, *i.e.*, from HCl coming from $NH_2OH{\cdot}HCl$, or humidity (either from the environment or from NH_2OH decomposition[29]). Carbon atoms in FG are susceptible to nucleophilic attack,[30] hence NH_2 radicals or NH_3 which are produced from the thermal decomposition of NH_2OH (Ref. 31) may act as nucleophiles and should be responsible for the high N content observed in pNG. Nevertheless, the prerequisite for nitrogen incorporation and doping into the graphene lattice is the formation of lattice vacancies. It has been shown that NH_3, NH_2 species,[32,33] or even R–NH_2 molecules[34] may attack graphene vacancies and edges resulting to N-doped graphenes, through a dehydrogenation mechanism.[32,33] But vacancies are usually formed by ion bombardment[34–36] or oxidation.[37] Therefore, a critical question in the present case pertains to the formation mechanism of vacancies in FG.

Stimulated by the appearance of C–H vibrations at 2859–2960 cm^{-1} on the IR spectrum of the by-product, we hypothesized that fragmentation of the carbon lattice might take place during the reaction at 130 °C. In order to shed more light, a reaction was performed in a ceramic crucible in a TGA system and evolved gases were monitored by mass spectroscopy. We observed that apart from defluorination (F fragments, m/z = 19), C–F (m/z = 31) fragments were also detected (see Figure S9A) at the temperature of the reaction (130 °C). On the contrary, when FG is subjected to thermal treatment in absence of hydroxylamine and solvent, F and CF fragments are released only above 400 and 600 °C, respectively (see Figure S9A, inset). The set of these data proved that carbonaceous fragments are released during synthesis of pNG, hence creating vacancies on the graphene lattice. The presence of the vacancies in pNG was also confirmed by IR and Raman spectroscopy. Theoretical calculations showed that a multi-vacancy is required for the ~1580 cm^{-1} aromatic ring band to appear (see Figure S7A–C). The Raman spectrum of pNG (see Figure S5B) displayed an intense D-band, corresponding to the presence of sp^3 carbons bonded to F (7.7 at. % of F was present in pNG, see Figure S4B), and to the presence of defects/vacancies. To verify this,

pNG was heat-treated at 900 °C, after which the Raman spectrum remained unchanged (see Figure S5B), although all fluorine atoms were removed, testifying the presence of vacancies.

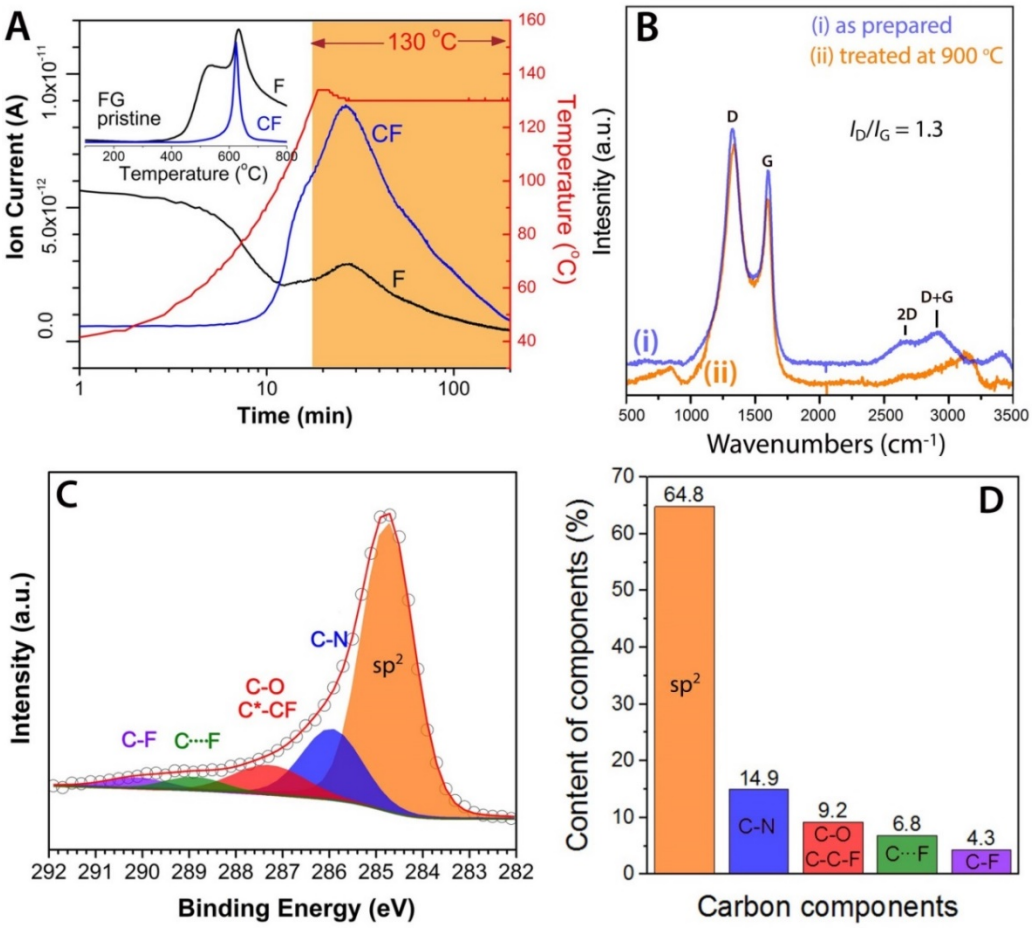

Figure S5. Structural insights on the preparation of the pyridinic nitrogen doped graphene. a) Released fragments during the reaction monitored with mass spectroscopy. The inset shows the fragments detected upon heating pristine FG powder. **b)** Raman spectra of (i) pNG and (ii) the same after heating at 900 °C under argon. The identical I_D/I_G ratio even after heating at 900 °C suggests that the D-band in the pNG sample did not originate from the fluorine-bonded sp^3 carbons, but from permanent lattice vacancies, not possible to be healed during heat treatment. **c)** Deconvolution of the C 1*s* HR-XPS spectrum from pNG. **d)** Contents of the different carbon environments obtained after deconvolution of the C 1*s* HR-XPS shown in panel (c), 64.8% from all carbon atoms are sp^2 hybridized corroborating the reductive defluorination and extended formation of C=C double bond network from FT-IR observations. The next carbon component (14.9 at. %) is ascribed to carbons bonded with nitrogen atoms, with binding energy centered at 285.9 eV, in accordance to previous findings for N-doped graphenes after NH_3-treatment.[38] The carbons bonded to F with a semi-ionic bond (C···F) were also evident at 289 eV, at lower binding energies than the covalently bonded C-F carbons (289.8 eV),[26,39] in accordance to the FT-IR findings. Oxygen detected in

the XPS elemental analysis is most probably ascribed to environmental contamination from adventitious components.[40,41] See also discussion reported later and Figure S9.

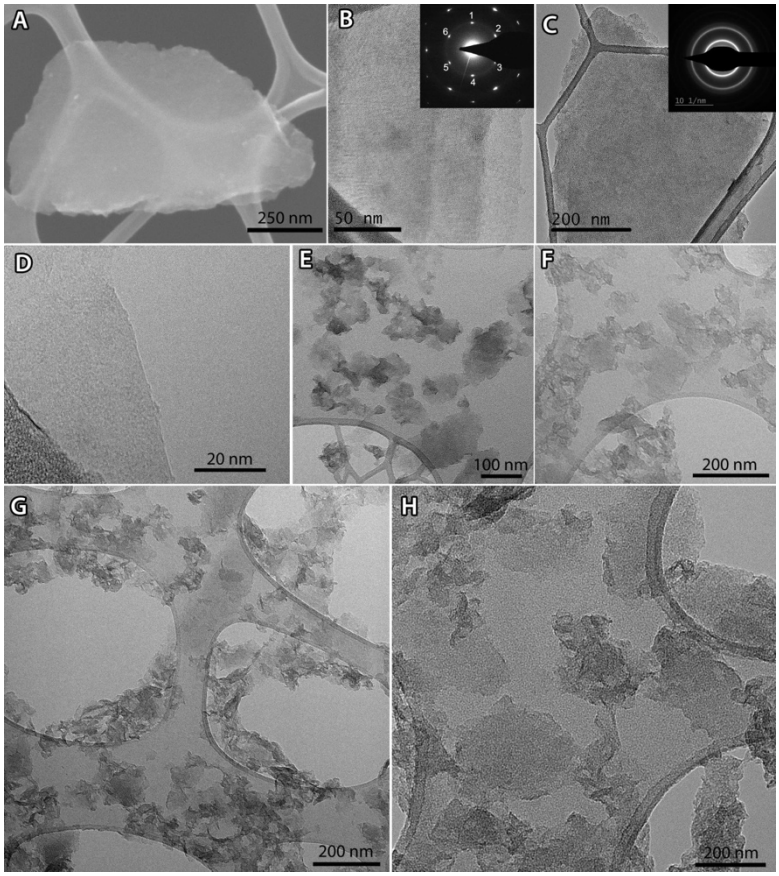

Figure S6. Electron microscopy characterization of the pyridinic nitrogen doped graphene. a) SEM image showing a transparent few-layer pNG flake. **b–h**) Transmission electron micrographs showing thin and transparent flakes, suggesting that pNG is mainly comprised of few-layered graphene sheets. Some of the flakes appear flat and others crumpled or folded. The lateral size is generally small, below 500 nm. The selected area diffraction pattern (SAED) in the inset of panel (b) shows intense diffraction spots of hexagonal symmetry, corresponding to the symmetry of graphene[42] and N-doped graphene.[43,44] The rings appearing are typically attributed to the decrease of crystallinity upon functionalization as well as overlying amorphous contamination.[44,45] The SAED pattern in the inset of panel (c) from a thicker flake shows concentric diffraction rings, suggesting that the individual sheets in the flake have random orientation, thus not forming a thick graphitic nanocrystal.

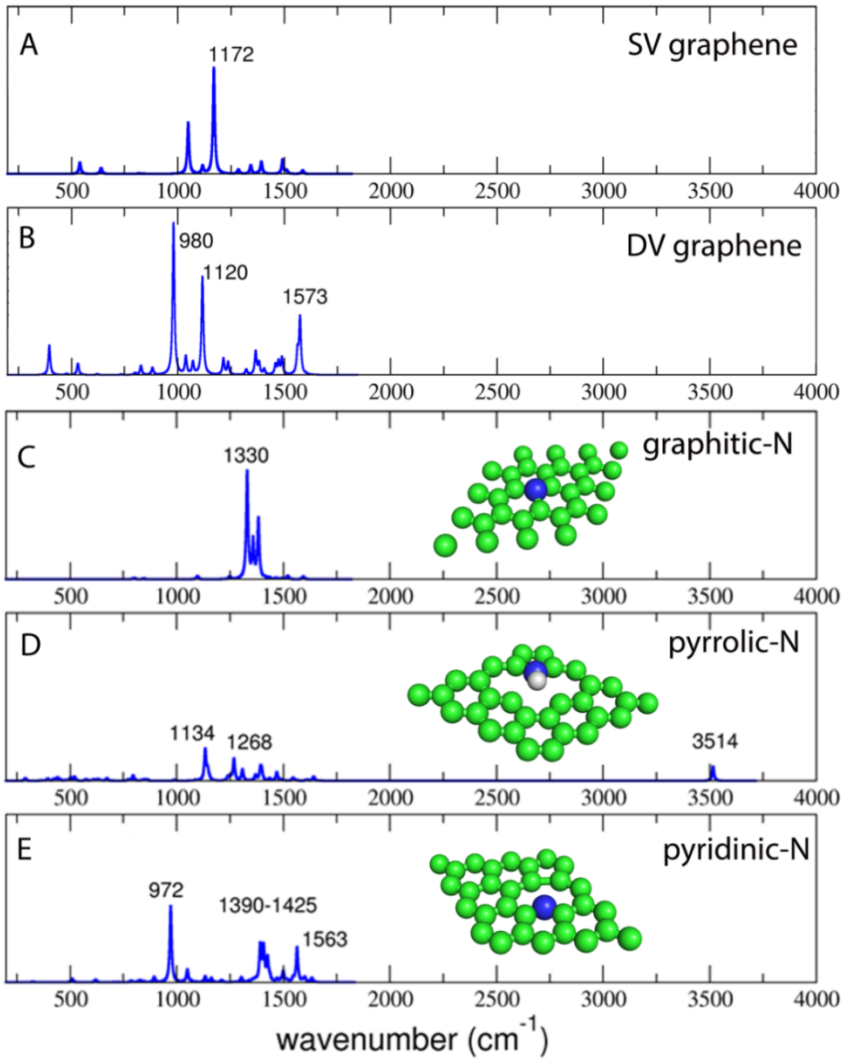

Figure S7. Theoretically calculated IR spectra of graphene adducts with mono and divacancies, as well as nitrogen-doped derivatives, where nitrogen atoms are placed in different configurations. Pyrrolic nitrogen motifs (-N-H) display the N-H vibration band above 3000 cm^{-1}, as known from IR textbooks, and as well theoretically calculated here in panel (d). Note: Panels c-e shows the recalculated IR envelopes fully consistent with those recently published in JPPC 2019 (P. Lazar, R. Mach, M. Otyepka *J. Phys. Chem. C,* **2019**, *123*(16), 10695-10702).

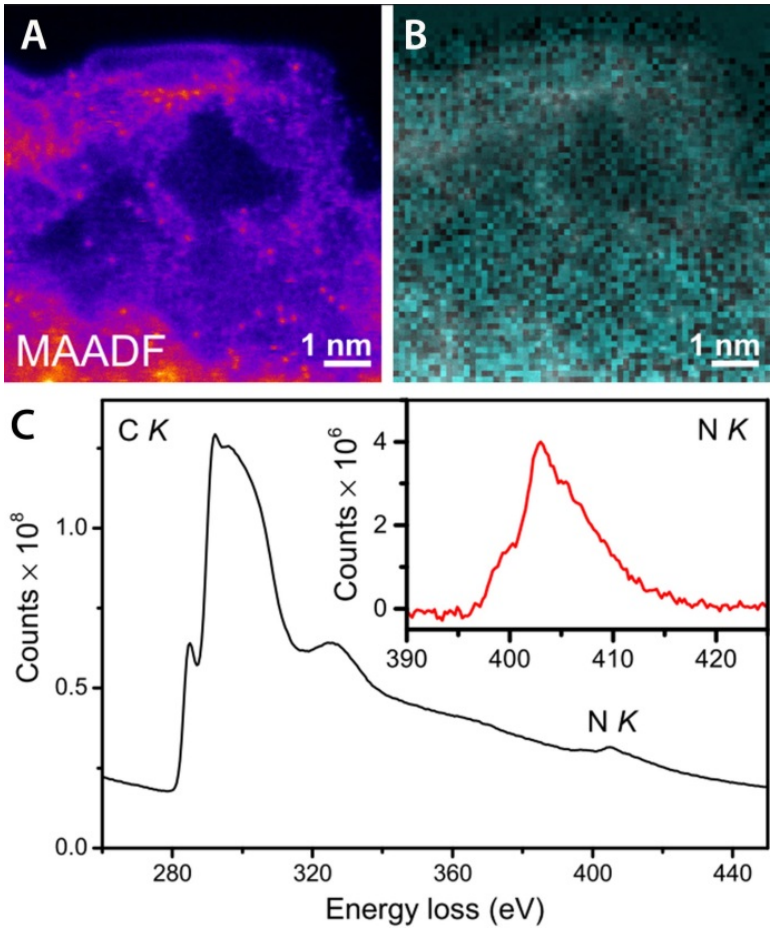

Figure S8. Probing the nature of nitrogen atoms in pNG with electron energy loss spectroscopy. a) STEM-MAADF image from near the edge of a pNG nanoflake and **b)** overlaid mapped signal from the background-subtracted N *K* edge signal, with **c)** showing the integrated spectrum over the field of view, inset with the N *K* signal consistent with predominantly pyridinic bonding.

Discussion on the O content. At similar wavenumbers of the C–F bond (1100 cm^{-1} in the IR spectrum of Figure S4D), C-O bands may also appear. Those of hydroxylic origin are excluded though, due to the absence of bands above 3300 cm^{-1}. It should be also noted that around 1100 cm^{-1} ring stretching vibrations of aromatic carbon rings and heterocyclic systems also appear.[11] Literature IR data show signals that are appearing in this region for non-fluorinated sp^2 carbon systems,[10,46-50] as well as for nitrogen-doped heterocyclic ones.[51,52] The etheric type C-O vibrations cannot be excluded, but since the amount of oxygen detected in the samples by XPS appears to be random, irrespective of the time of the reaction (see Figure S4B), we suggest that this oxygen comes from the environment and is not structural oxygen of pNG.

Oxygen adsorption on graphitic structures is known to persist even at very low pressure.[53] For instance, when *in situ* XPS is performed on magnetron-sputtered carbon nitride thin films, no oxygen is detected in the sample, while the same sample after exposure in atmosphere displays 5% of oxygen.[54] Further evidence for the environmental origin of oxygen can be derived from TGA-MS analysis of the sample under Ar atmosphere (see Figure S9A), where we monitored the oxygen-containing evolved species. According to the results, there is only desorption of H_2O and OH at very low temperature (below 200 °C), which can be ascribed to adsorbed humidity. If structural oxygen would be present, then species such as CO_2 and NO should be expected in the spectra at higher temperatures due to the oxidative decomposition products of the N-doped graphene, as indeed they appear when the same experiment is performed under synthetic air (see Figure S9B).

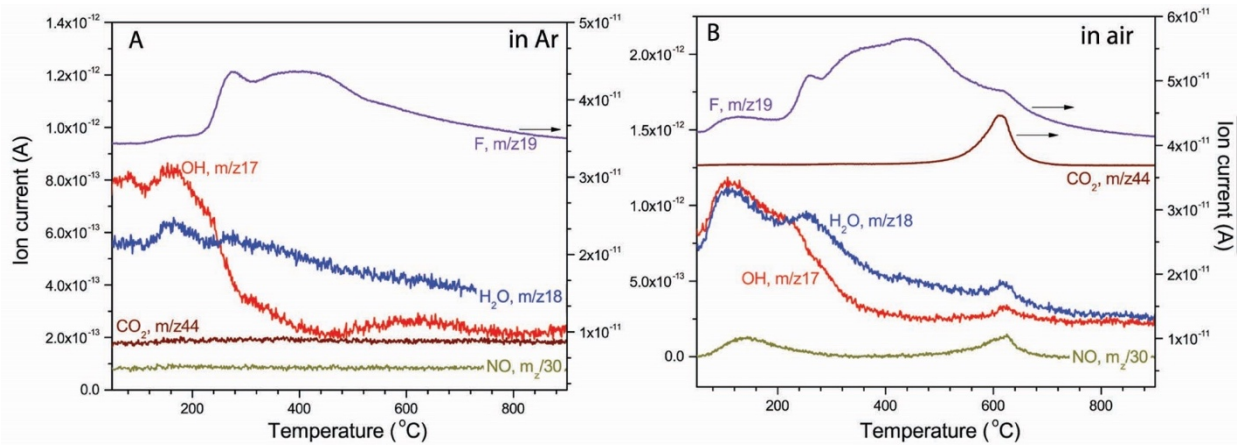

Figure S9. Mass spectra of evolved gasses during thermogravimetric analysis of pNG. a) TGA-MS traces of the studied N-doped graphene recorded under Ar atmosphere and **b)** synthetic under air. The curves have been shifted for better clarity.

Comments on the zeta potential and the XPS spectra of pNG (Figure 2F in the main text). Nitrogen doping through NH_3 dehydrogenation in graphene vacancies may result into pyridinic, pyrrolic, or graphitic configurations. Pyridinic nitrogens are basic chemical groups, because the electron lone pair located in p_x-like non-bonding orbital[55] is not part of the aromatic system and is free to bind protons and thus turn positively charged.[56] In contrast, pyrrolic nitrogens share their lone electron pair of the unhybridized p_z orbital with the rest four electrons of the four carbons in the ring to attain aromaticity, thus with no tendency for protonation.[57] Therefore, pyridine is a base with pK_a of the conjugate acid of 5.2 (Ref. 57) and pyrrole is not, with a pK_a of ~0. For these reasons, pyridinic nitrogens in graphitic structures have been suggested to induce Lewis basicity.[35,57] Exploiting these properties, we measured the zeta potential of the product at various pH values (see Figure 2F). Below pH of ~5, the pNG flakes acquired highly positive surface charge (over +30 mV at pH = 3) due to protonation. On the contrary, the zeta potential of pyrrole-based systems is, as expected, negative.[58,59]

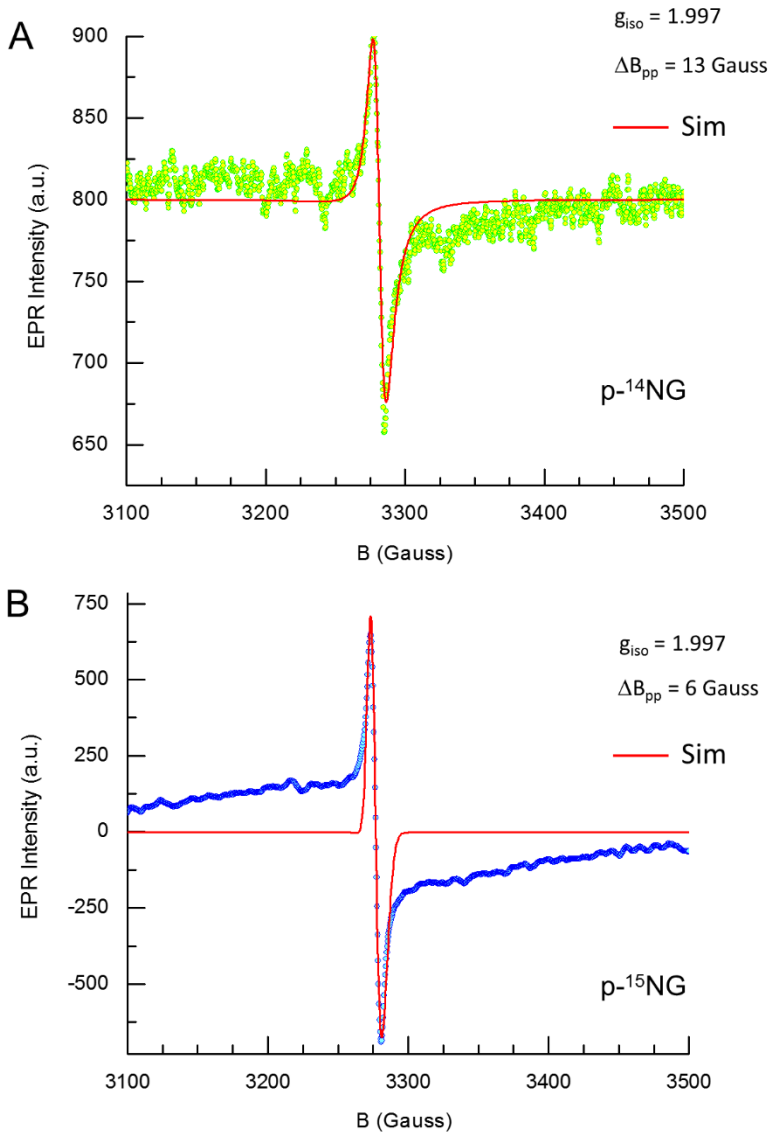

Figure S10. Low temperature X-band EPR spectra. a) p-^{14}NG and **b)** p-^{15}NG recorded T = 118 K and in the narrow field-sweep region (around g = 2.00). Experimental settings: 100 kHz modulation frequency, 2.0 Gauss modulation width, 2 min sweep time, 0.03 s time constant and recorded with 0.3 mW microwave power. Two scans were accumulated and averaged. The red traces in (a) and (b) correspond to the S = 1/2 simulation of the EPR transition related to the narrow signal (Lorentzian component, S_L).

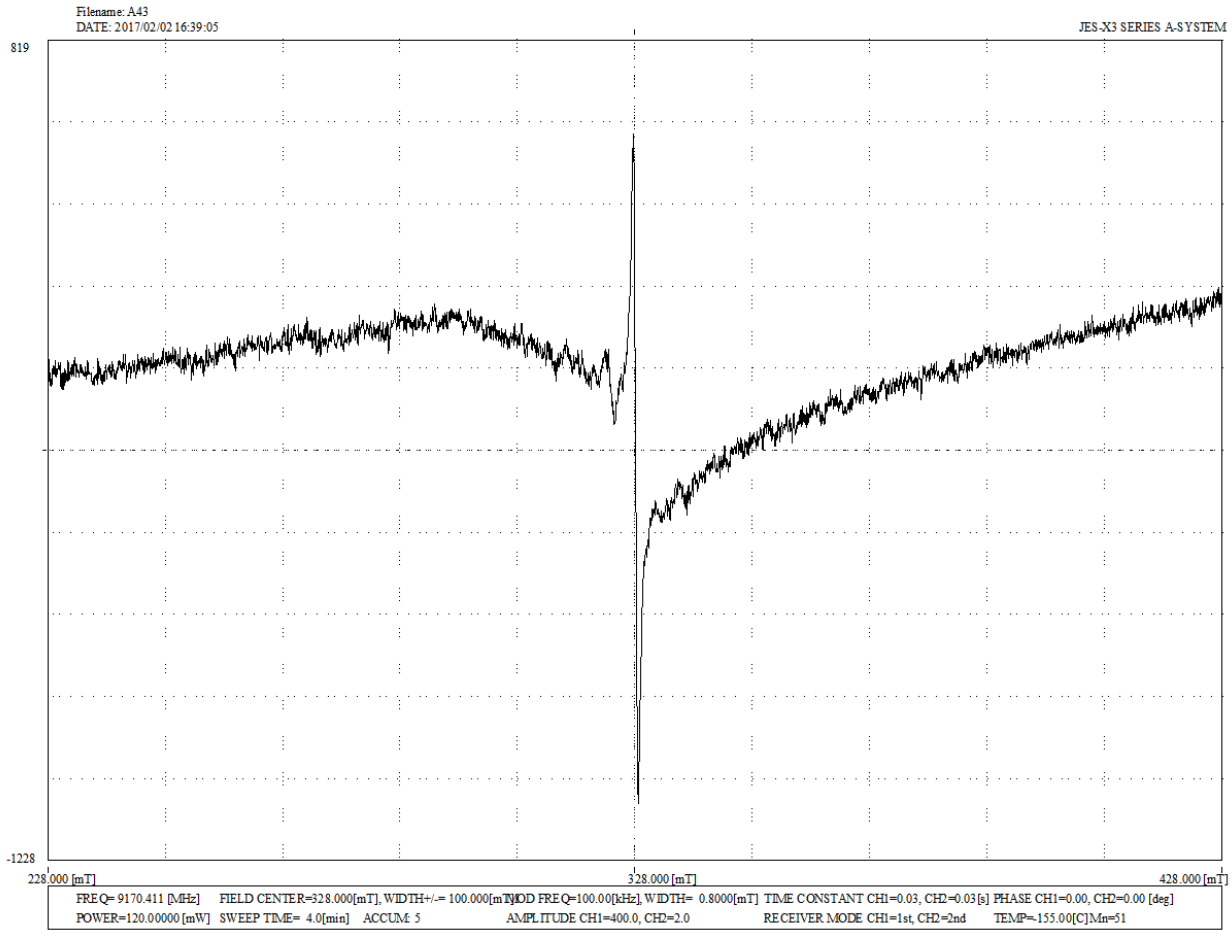

Figure S11. X-band EPR spectrum of p-^{14}NG recorded at T = 118 K and at high power (120 mW). Experimental settings are given in the spectrum plot.

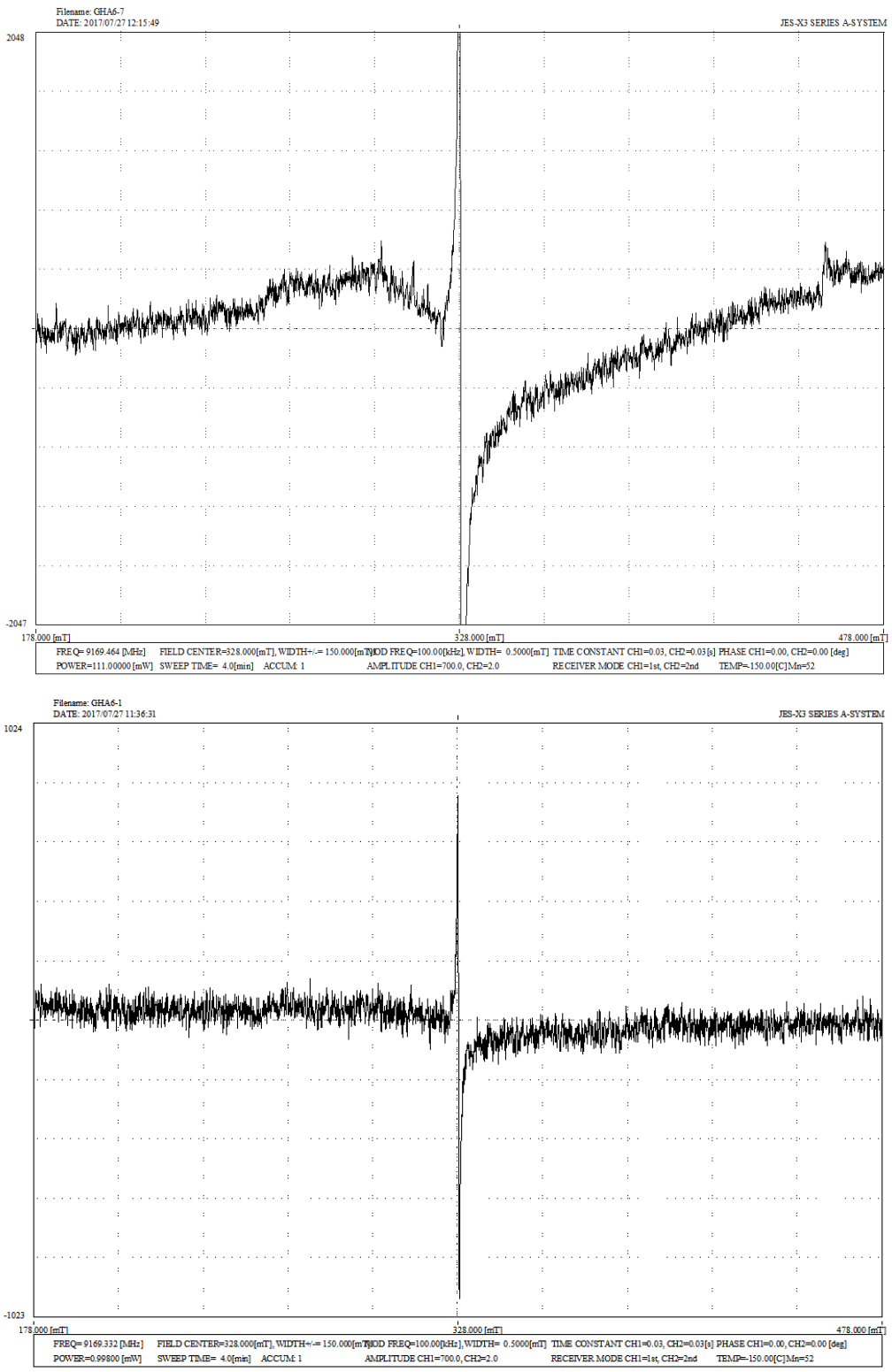

Figure S12. X-band EPR spectrum of p-^{14}NG recorded at T = 123 K and at high power (111 mW, upper trace) compared to the low-power spectrum (1.0 mW, lower trace). Experimental settings: 0.5 mT modulation width, 4 min sweep time, 0.03 s time constant.

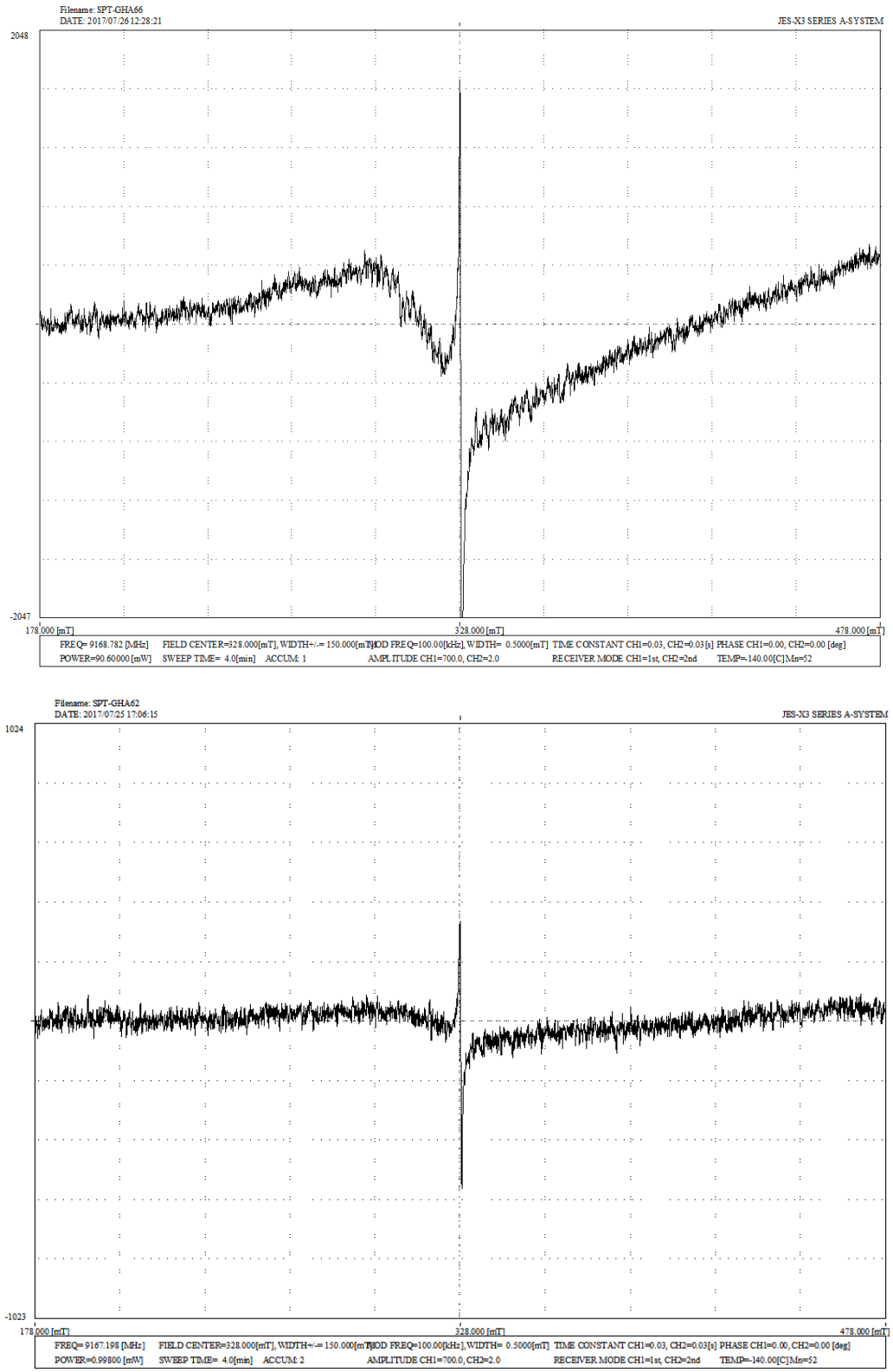

Figure S13. X-band EPR spectrum of p-^{14}NG recorded at T = 133 K and at high power (90.6 mW, upper trace) compared to the low-power spectrum (1.0 mW, lower trace). Experimental settings: 0.5 mT modulation width, 4 min sweep time, 0.03 s time constant.

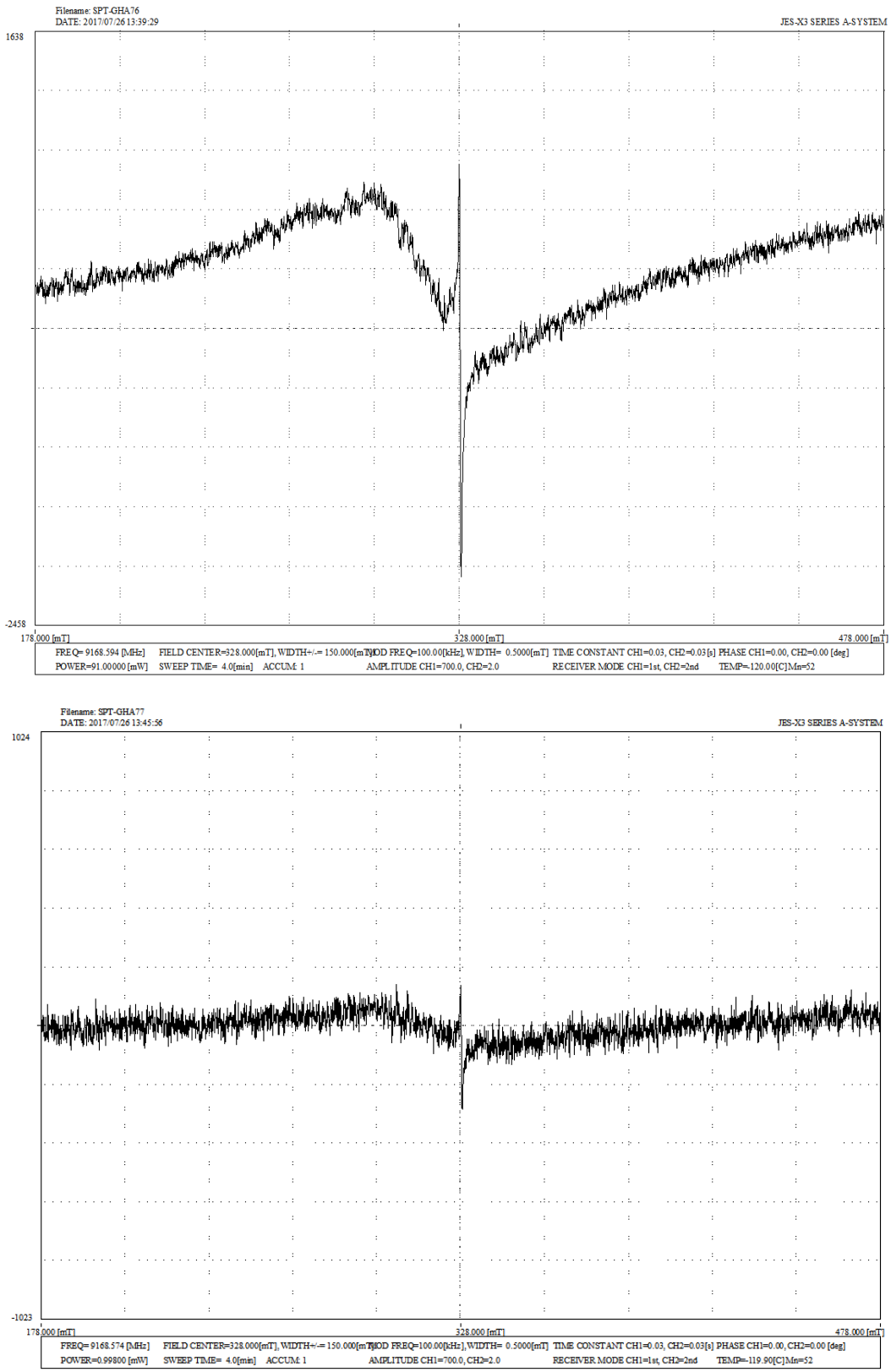

Figure S14. X-band EPR spectrum of p-^{14}NG recorded at T = 153 K and at high power (91 mW, upper trace) compared to the low-power spectrum (1.0 mW, lower trace). Experimental settings: 0.5 mT modulation width, 4 min sweep time, 0.03 s time constant.

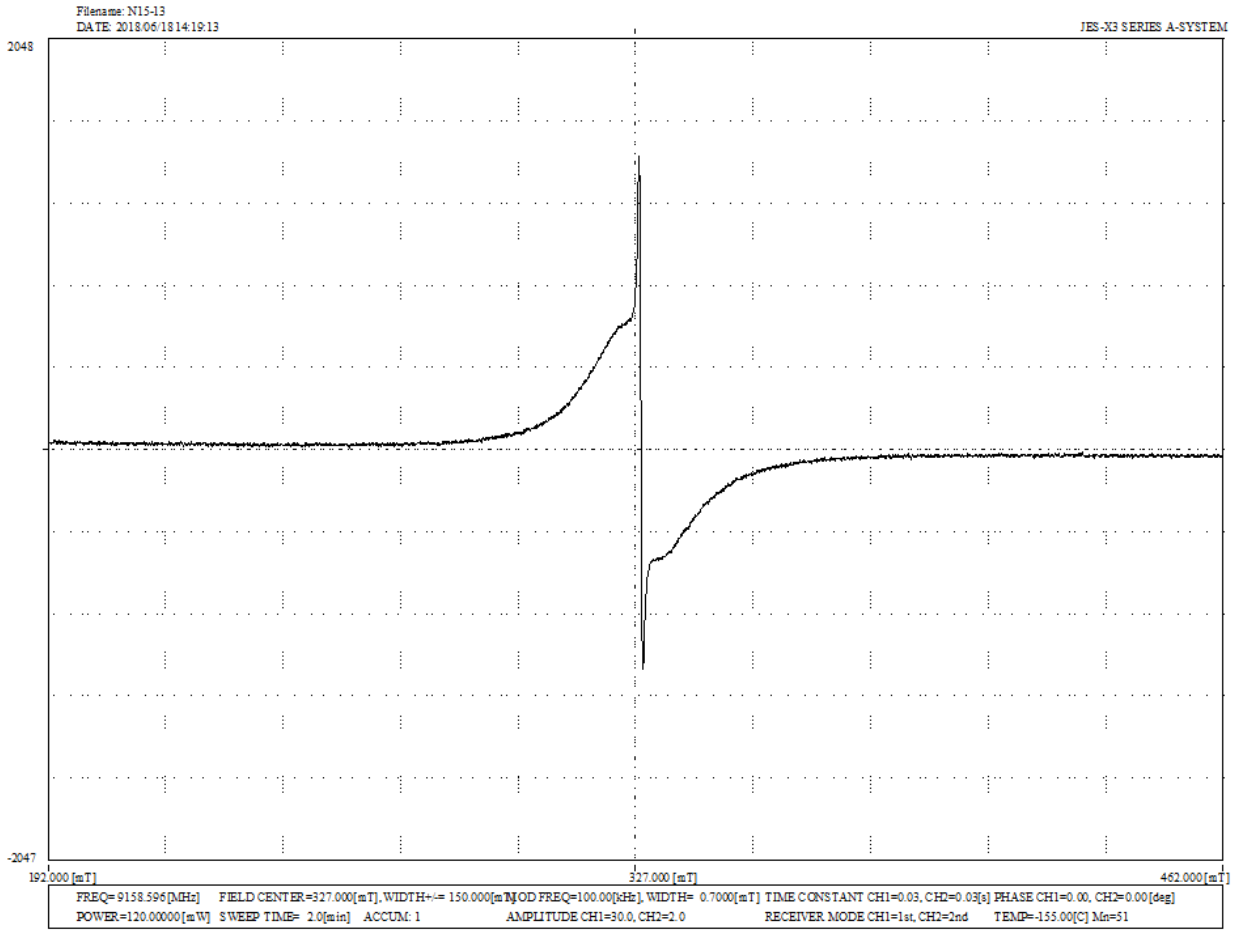

Figure S15. X-band EPR spectrum of p-^{15}NG recorded at T = 118 K and at high power (120 mW). Experimental settings are given in the spectrum plot.

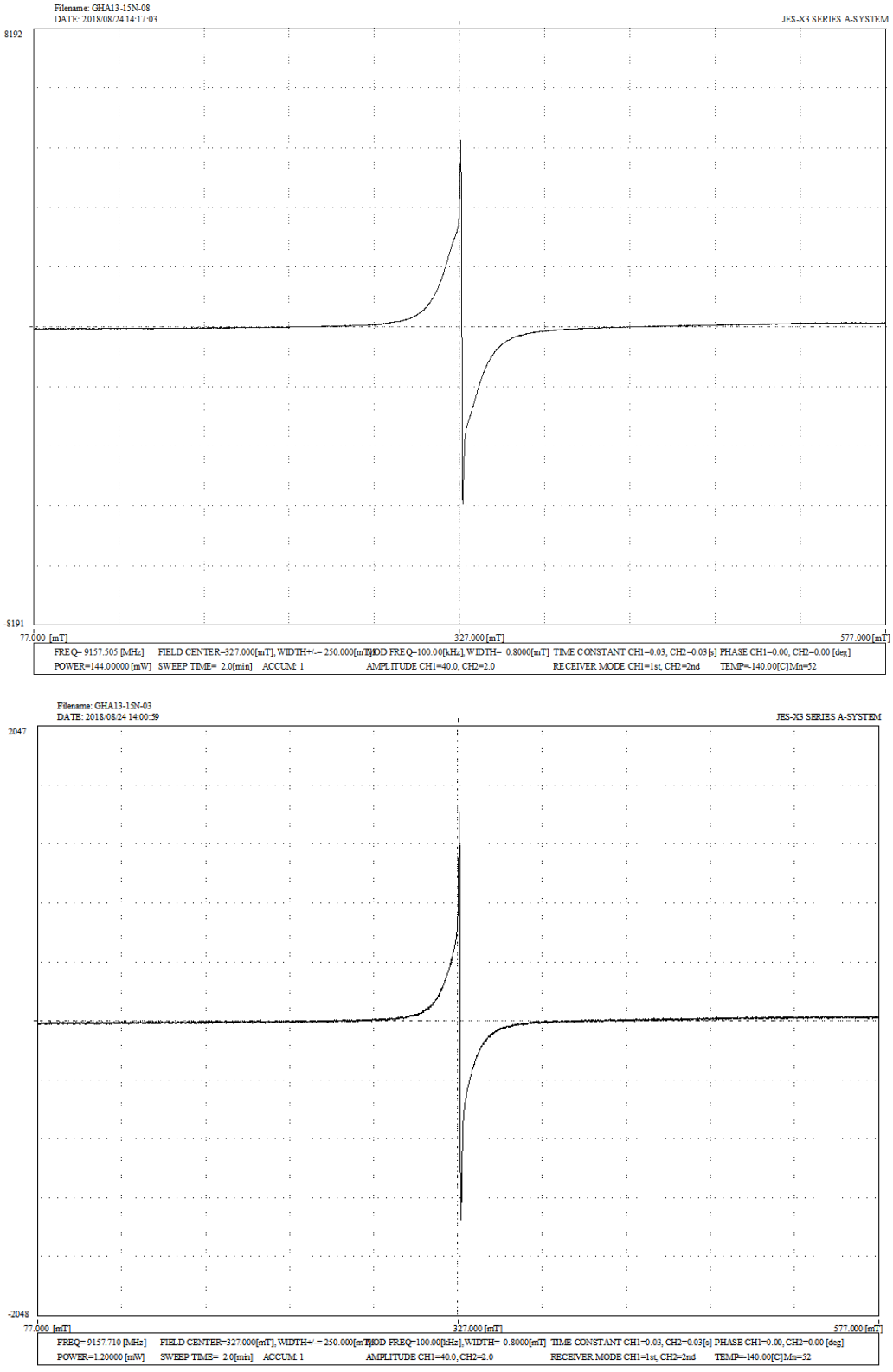

Figure S16. X-band EPR spectrum of p-^{15}NG recorded at T = 133 K and at high power (144 mW, upper trace) compared to the low-power spectrum (1.2 mW, lower trace). Experimental settings: 0.8 mT modulation width, 2 min sweep time, 0.03 s time constant.

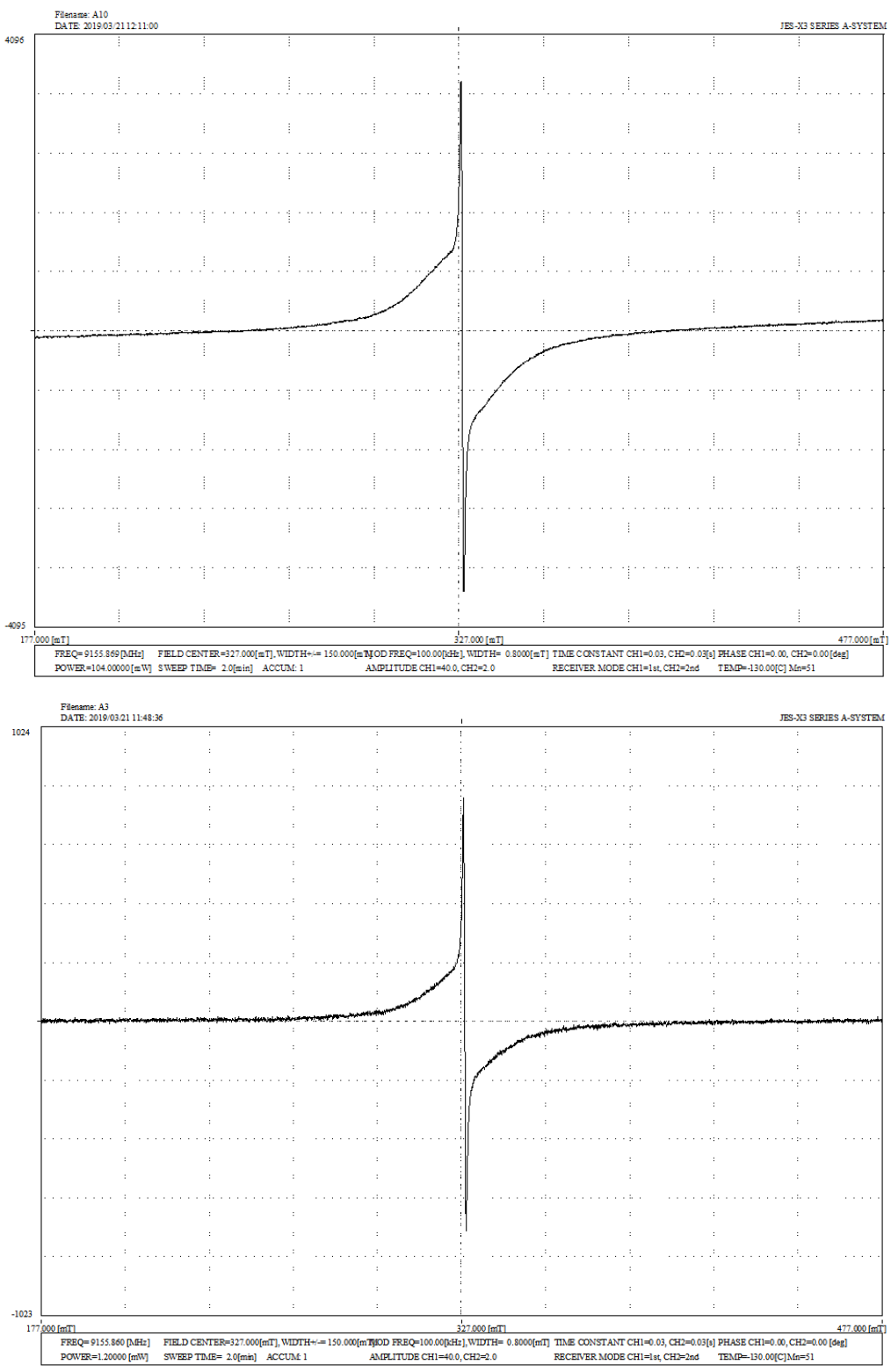

Figure S17. X-band EPR spectrum of p-^{15}NG recorded at T = 143 K and at high power (104 mW, upper trace) compared to the low-power spectrum (1.2 mW, lower trace). Experimental settings: 0.8 mT modulation width, 2 min sweep time, 0.03 s time constant.

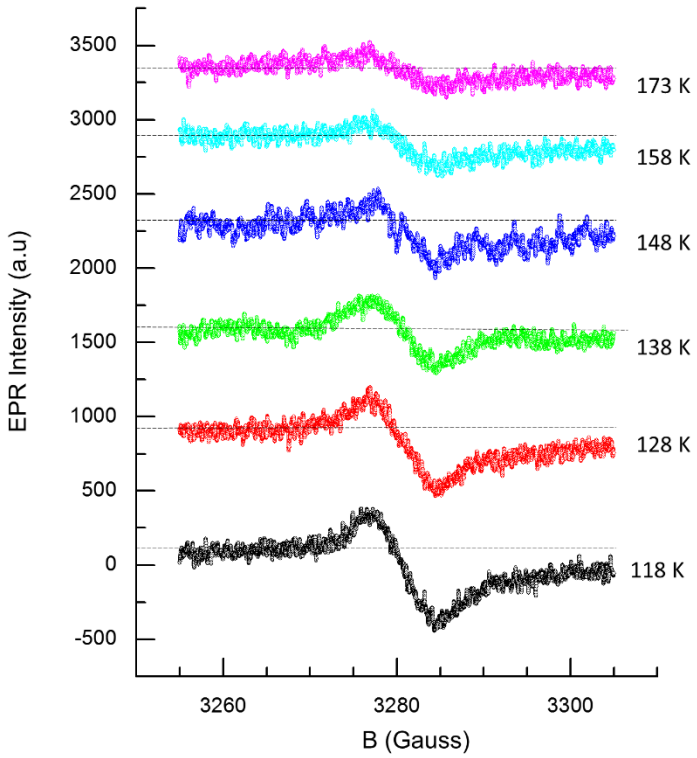

Figure S18. X-band EPR spectra (9.172 GHz) of p-^{14}NG recorded around the g = 2 region at various temperatures. The large asymmetry in the signal is evidenced with the use of a dotted baseline. Experimental settings: 100 kHz modulation frequency, 4.0 Gauss modulation width, 2 min sweep time, 0.03 s time constant and 0.3 mW microwave power. Four scans were accumulated and averaged. Spectra are displayed by vertical shift.

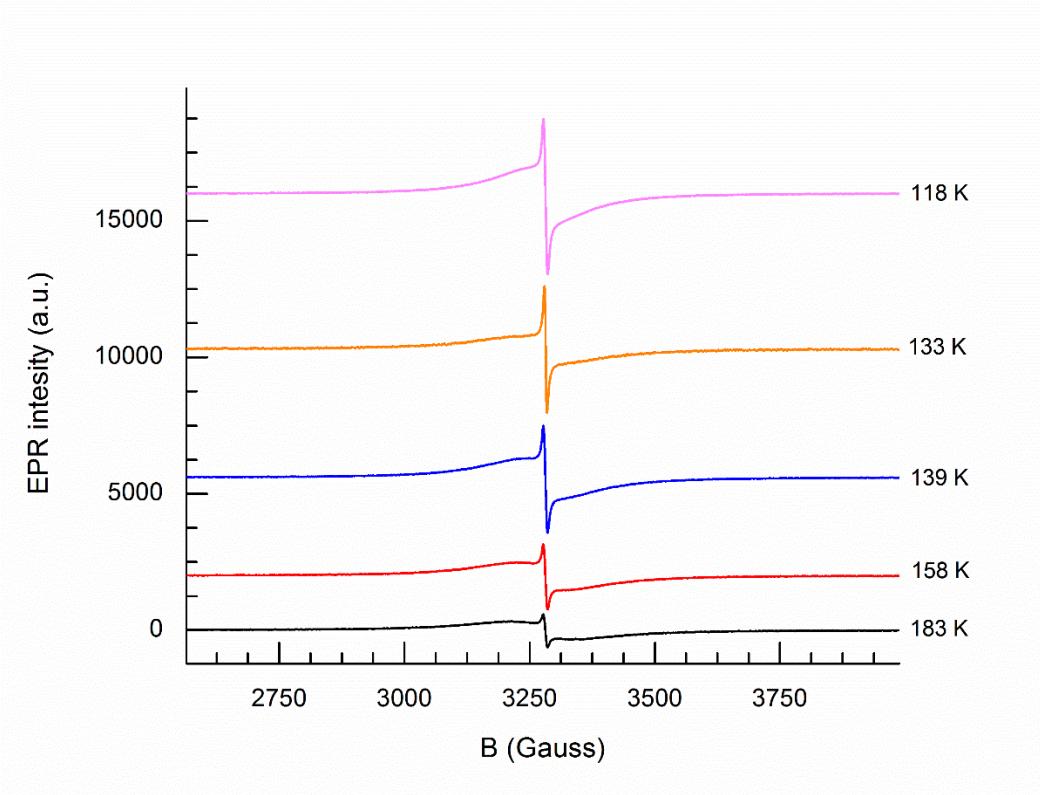

Figure S19. X-band EPR spectra (9.160 GHz) of p-^{15}NG recorded at various temperatures. Experimental settings: 100 kHz modulation frequency, 7.0 Gauss modulation width, 2 min sweep time, 0.03 s time constant and 0.8 mW microwave power. Spectra are displayed by vertical shift.

Comments on the results from bulk magnetic susceptibility measurements. Both the Curie law and Curie-Weiss law failed to fit correctly the profile of χ_{mass} in the whole temperature range, implying the presence of two or more fractions behaving in a different magnetic manner. Moreover, the existence of the inflection point in χ_{mass} (at ~79 K) evidenced for a magnetic transition to a ferromagnetic state upon lowering the temperature. Thus, it was hypothesized that the pNG sheets showed two magnetically different regions, *i.e.*, domains with significant magnetic interactions, promoting ferromagnetic ordering at low temperatures, and paramagnetic regions where magnetic moments are either non-interacting or interacting very weakly due to presence of conduction (itinerant) electrons. Assuming that the ferromagnetic component, $\chi_{mass,ferro}$, saturates at low temperatures and the paramagnetic fraction strictly follows the modified Curie law ($\chi_{mass,para} = \chi_{para,non} + \chi_P = C/T + \chi_P$, where C is the Curie constant, T is the temperature, and χ_P is the Pauli paramagnetic susceptibility, temperature-independent in the degenerate limit), the temperature evolution of $\chi_{mass,ferro}$ could be deduced by subtracting $\chi_{mass,para}$ from χ_{mass} (see inset in Figure S20A). Thus, the inflection point observed in χ_{mass} could be ascribed to the Curie temperature, T_C, when respective regions passed from the paramagnetic state to the ferromagnetic regime. In other words, the ferromagnetic contribution reflected the presence of strong exchange regime, as concluded from the analyses of the EPR spectra. The establishment of ferromagnetic ordering was further confirmed by the hysteresis character of the isothermal magnetization curve at 5 K (see inset in Figure S20B,C) with nonzero values of coercivity and remanent magnetization. The hysteresis loop does not show saturation at high applied magnetic fields (up to 50 kOe) due to the dominant paramagnetic component. On the other hand, the paramagnetic response featured two contributions, *i.e.*, one originating from the non-interacting localized magnetic moments (mostly located on carbon atoms, $\chi_{para,non} = C/T$) and the second (assumed as temperature-independent, χ_P) from conduction (itinerant) electrons. Here, it should be mentioned that Pauli paramagnetism is generally a weak effect, which is much smaller compared to the response of non-interacting paramagnetic centers with at least one unpaired electron localized on them. This is because in paramagnetic materials, at least one electron on every magnetic atom contributes to χ_{mass}, but in a metal, it is only those electrons close to the Fermi surface which play a role. That is why $\chi_{para,non}$ dominates at low temperatures while χ_P becomes evident at higher temperatures (see inset in Figure S20). Therefore, from the bulk magnetization data, the coexistence of the two different spin populations was confirmed, one from localized magnetic moments (*i.e.*, a ferromagnetic contribution) and the other one,

besides non-interacting magnetic moments, stemming from conduction (itinerant) electrons (*i.e.*, a paramagnetic contribution), corroborating thus the finding from EPR technique.

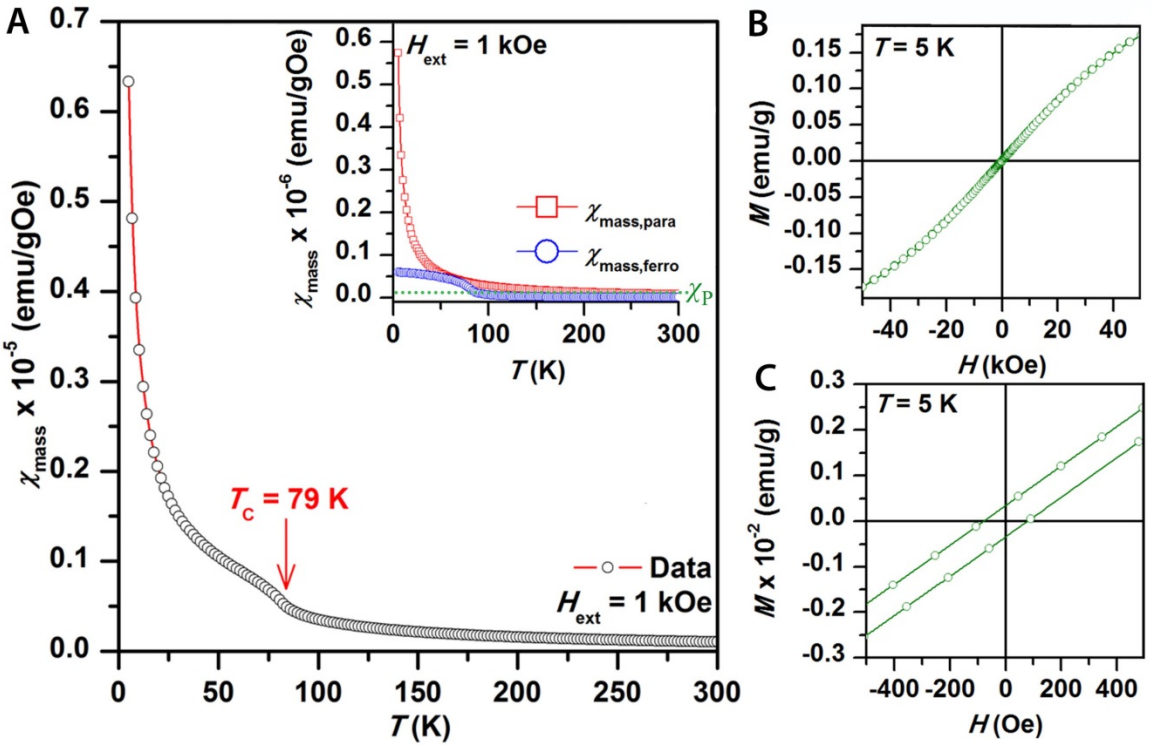

Figure S20. Magnetization behavior of p-^{14}NG. a) Temperature evolution of mass magnetic susceptibility, χ_{mass}, of the pNG sample, measured under and external magnetic field of 1 kOe. The insets show the behavior of mass magnetic susceptibility for paramagnetic, $\chi_{mass,para}$, and ferromagnetic, $\chi_{mass,ferro}$, fraction as a function of temperature. T_C stands for the Curie temperature. **b)** Hysteresis loop of the pNG sample recorded at a temperature of 5 K and **c)** profile of the collected hysteresis loop around the origin.

POWER-SATURATION SPECTRA OF p-^{15}NG

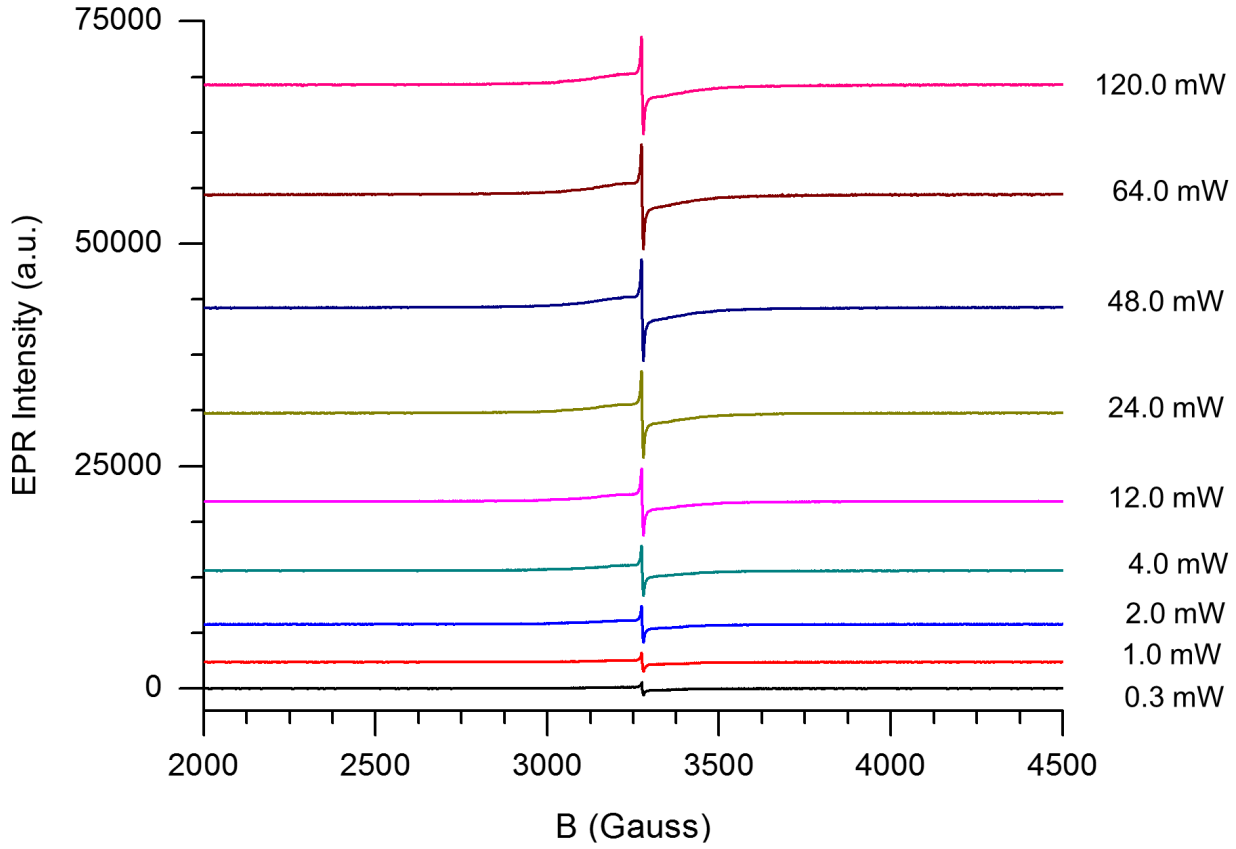

Figure S21. X-band EPR spectra (9.159 GHz) of p-^{15}NG recorded at various microwave powers at T = 118 K. Experimental settings: 100 kHz modulation frequency, 7.0 Gauss modulation width, 2 min sweep time, 0.03 s time constant. Spectra are displayed by vertical shift.

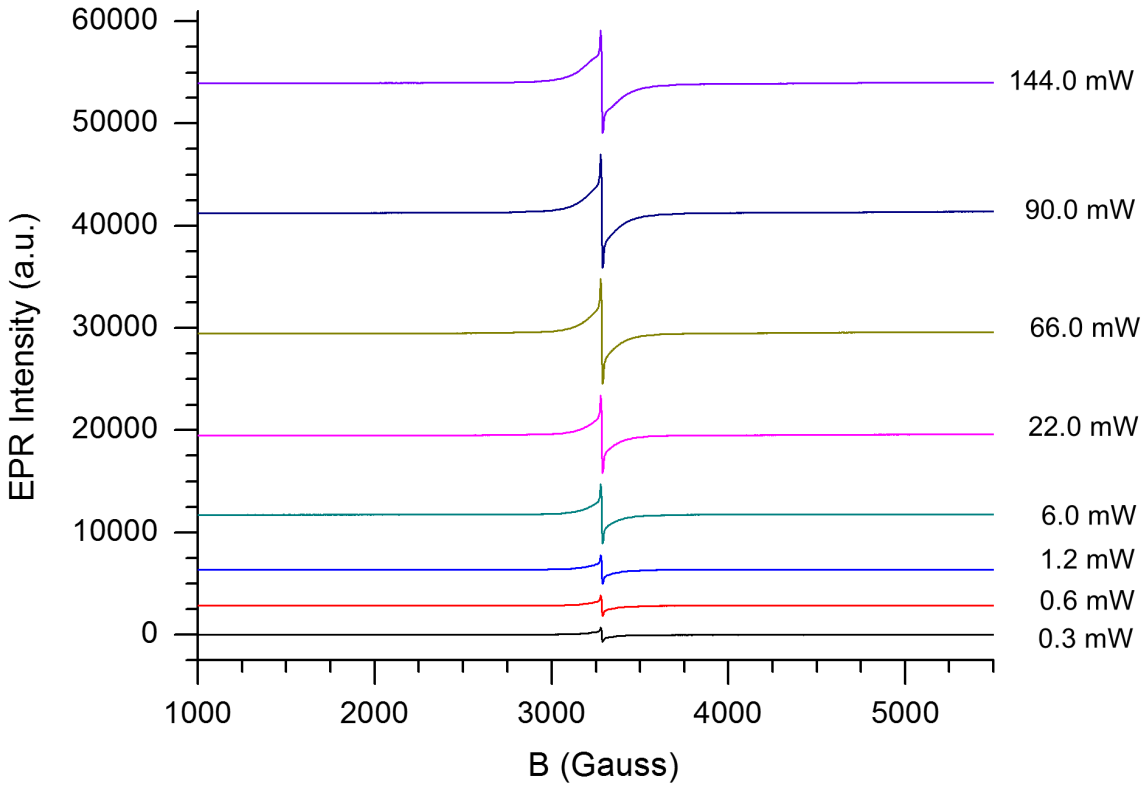

Figure S22. X-band EPR spectra (9.154 GHz) of p-^{15}NG recorded at various microwave powers at T = 133 K. Experimental settings: 100 kHz modulation frequency, 2.5 Gauss modulation width, 4 min sweep time, 0.03 s time constant. Spectra are displayed by vertical shift.

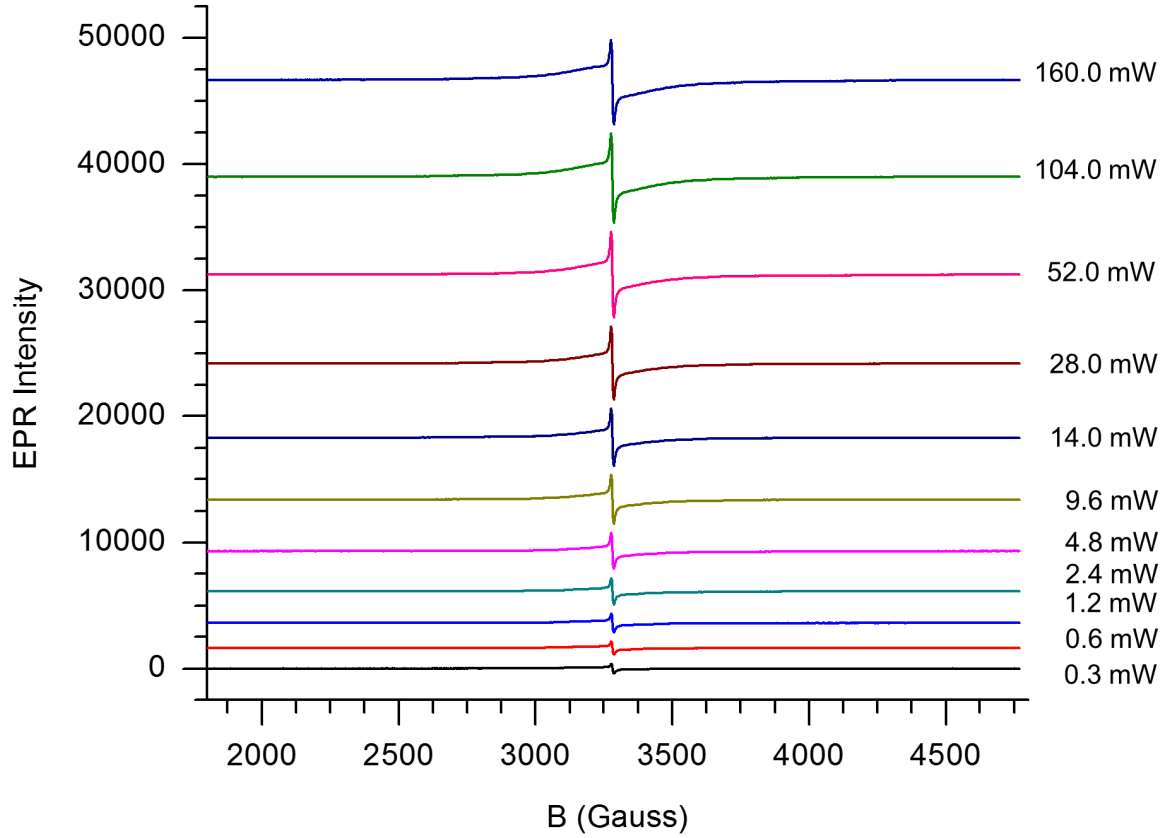

Figure S23. X-band EPR spectra (9.156 GHz) of p-^{15}NG recorded at various microwave powers at T = 143 K. Experimental settings: 100 kHz modulation frequency, 8.0 Gauss modulation width, 2 min sweep time, 0.03 s time constant. Spectra are displayed by vertical shift.

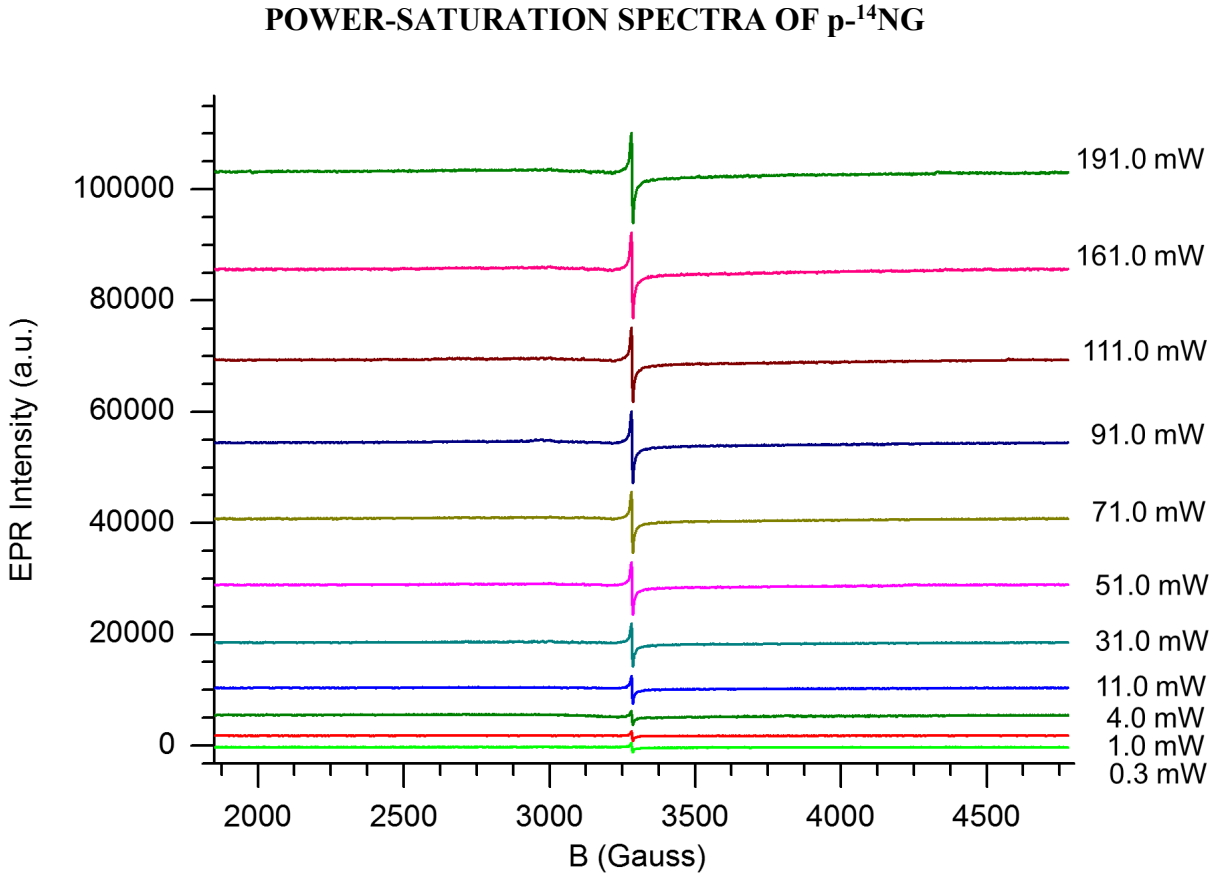

Figure S24. X-band EPR spectra (9.169 GHz) of p-^{14}NG recorded at various microwave powers at T = 123 K. Experimental settings: 100 kHz modulation frequency, 5.0 Gauss modulation width, 2 min sweep time, 0.03 s time constant. Spectra are displayed by vertical shift.

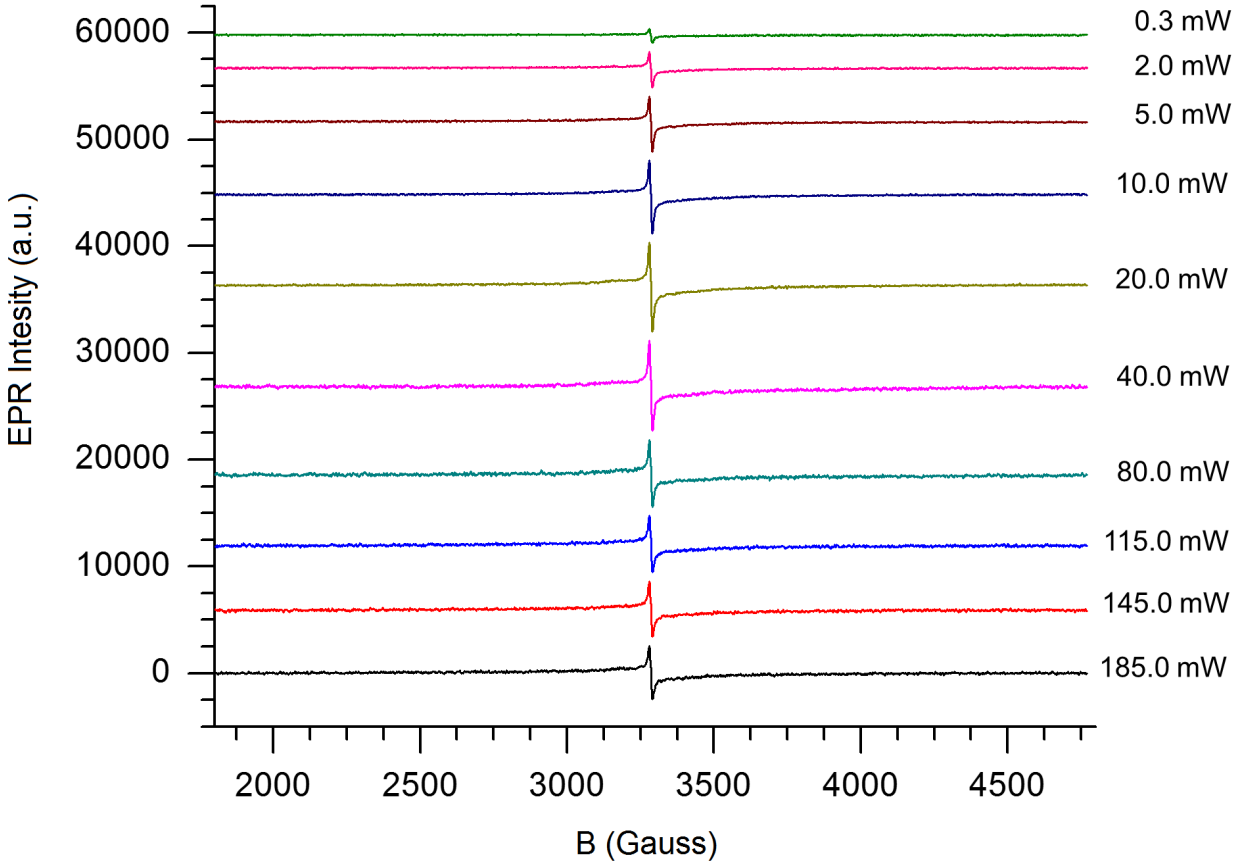

Figure S25. X-band EPR spectra (9.165 GHz) of p-^{14}NG recorded at various microwave powers at T = 133 K. Experimental settings: 100 kHz modulation frequency, 10.0 Gauss modulation width, 2 min sweep time, 0.03 s time constant. Spectra are displayed by vertical shift.

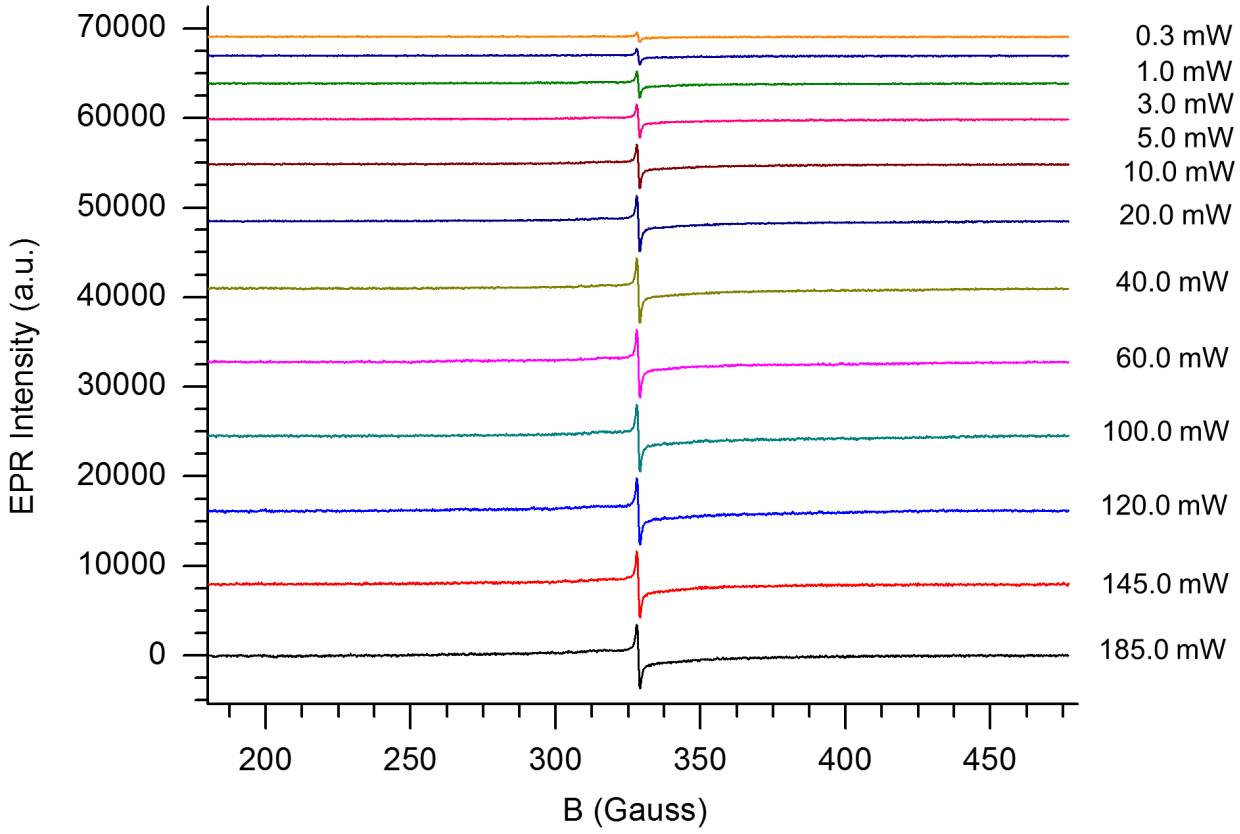

Figure S26. X-band EPR spectra (9.166 GHz) of p-^{14}NG recorded at various microwave powers at T = 143 K. Experimental settings: 100 kHz modulation frequency, 10.0 Gauss modulation width, 2 min sweep time, 0.03 s time constant. Spectra are displayed by vertical shift.

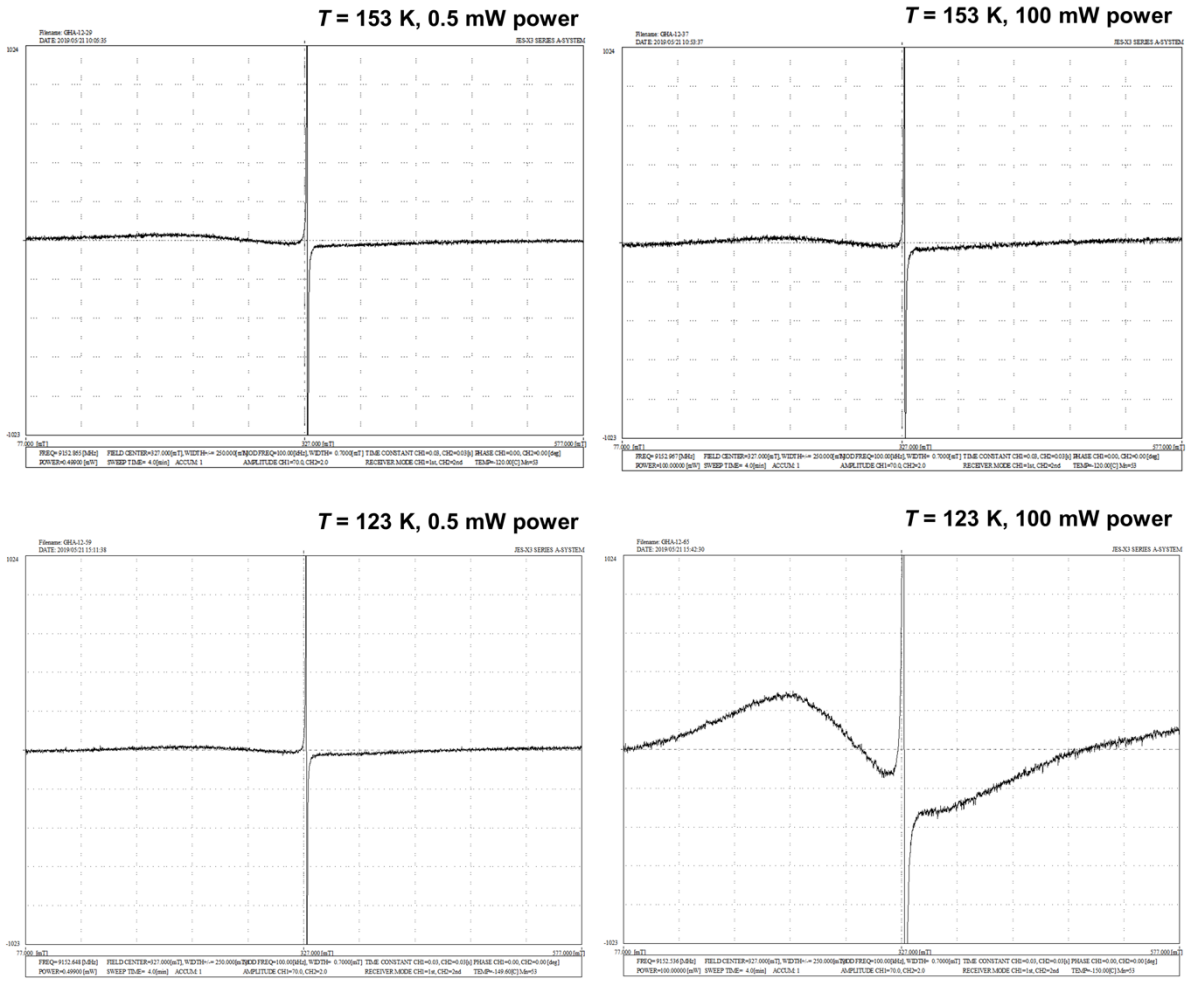

Figure S27. X-band EPR spectra of a third batch of as-synthesized p-^{14}NG material recorded at various microwave powers and temperatures. Experimental settings are reported in the spectra plots and are shown as recorded.

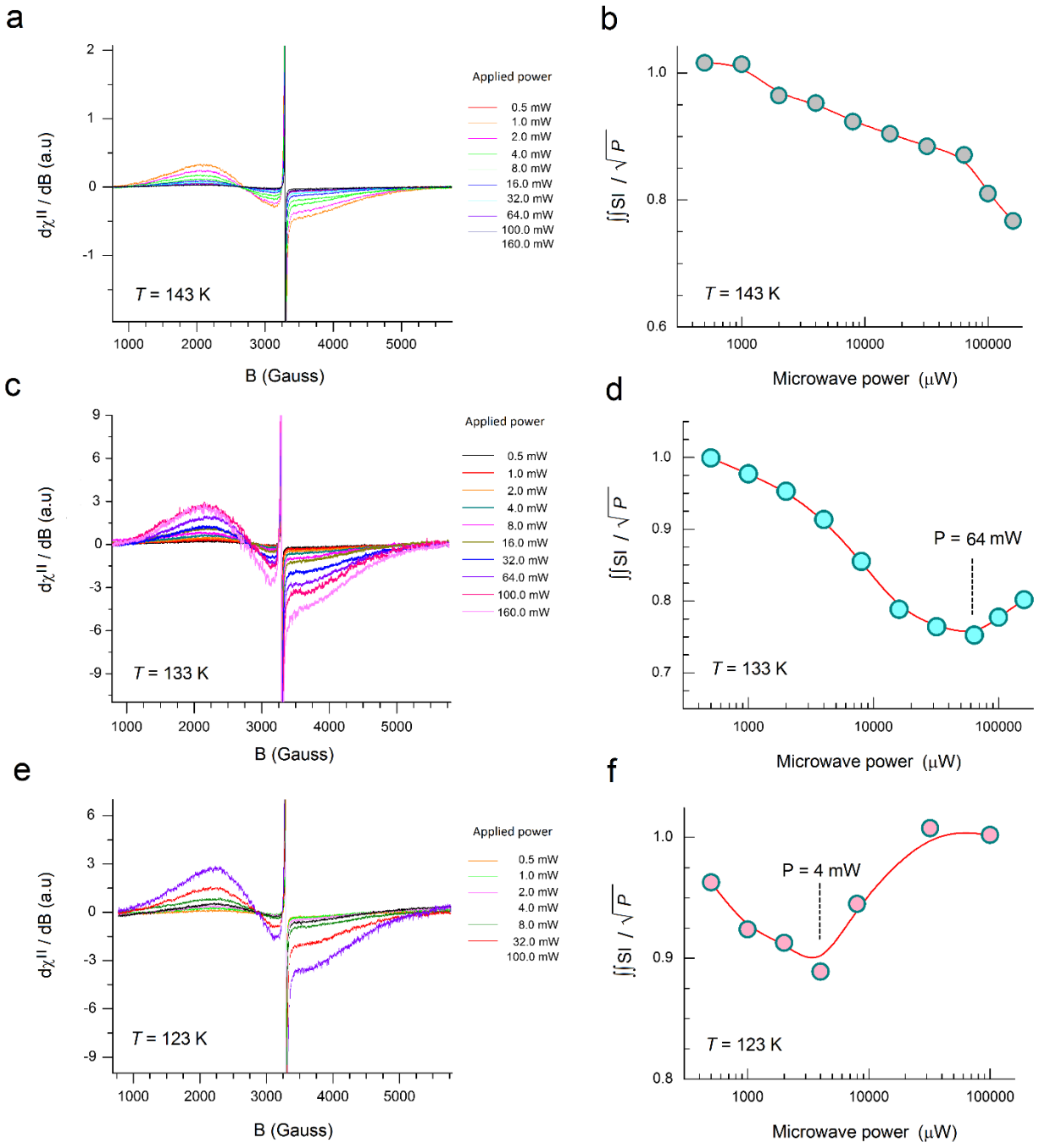

Figure S28. X-band EPR spectra of a third batch of as-synthesized p-^{14}NG recorded at various microwave powers and at various temperatures (**a**, T= 143 K; **c**, T = 133 K; **e**, T = 123 K). Experimental settings: 100 kHz modulation frequency, 0.7 Gauss modulation width, 4 min sweep time, 0.03 s time constant. Panels **b**, **d**, **f** show the correspondent saturation plots at various temperatures (**b**, T= 143 K; **d**, T = 133 K; **f**, T = 123 K), expressed as double integrated signal intensities of the spectra shown in panels **a**, **c**, **e** divided by the square root of the applied powers and normalized.

Supplementary references

(1) Susi, T.; Hardcastle, T. P.; Hofsäss, H.; Mittelberger, A.; Pennycook, T. J.; Mangler, C.; Drummond-Brydson, R.; Scott, A. J.; Meyer, J. C.; Kotakoski, J. Single-Atom Spectroscopy of Phosphorus Dopants Implanted into Graphene. *2D Mater.* **2017**, *4* (2), 021013.

(2) Korb, J.-P.; Maruani, J. A Fast Deconvolution Procedure for Inhomogeneous Bell-Shaped Lines and its Application to Spin-Relaxation Studies. *J. Magn. Reson.* **1982**, *46* (3), 514–520.

(3) Lund, A.; Sagstuen, E.; Sanderud, A.; Maruani, J. Relaxation-Time Determination from Continuous-Microwave Saturation of EPR Spectra. *Radiat. Res.* **2009**, *172*, 753–760.

(4) Kresse, G.; Furthmüller, J. Efficient Iterative Schemes for *Ab Initio* Total-Energy Calculations Using a Plane-Wave Basis Set. *Phys. Rev. B* **1996**, *54*, 11169–11186.

(5) Kresse, G.; Joubert, D. From Ultrasoft Pseudopotentials to the Projector Augmented-Wave Method. *Phys. Rev. B* **1999**, *59*, 1758–1775.

(6) Blöchl, P. E. Projector Augmented-Wave Method. *Phys. Rev. B* **1994**, *50*, 17953–17979.

(7) Perdew, J. P.; Burke, K.; Ernzerhof, M. Generalized Gradient Approximation Made Simple. *Phys. Rev. Lett.* **1996**, *77*, 3865–3868.

(8) Blöchl, P. E.; Jepsen, O.; Andersen, O. K. Improved Tetrahedron Method for Brillouin-Zone Integration. *Phys. Rev. B* **1994**, *49*, 16223–16233.

(9) Lin, Y.-C.; Teng, P.-Y.; Yeh, C.-H.; Koshino, M.; Chiu, P.-W.; Suenaga, K. Structural and Chemical Dynamics of Pyridinic-Nitrogen Defects in Graphene. *Nano Lett.* **2015**, *15* (11), 7408–7413.

(10) Bakandritsos, A.; Pykal, M.; Błoński, P.; Jakubec, P.; Chronopoulos, D. D.; Poláková, K.; Georgakilas, V.; Čépe, K.; Tomanec, O.; Ranc, V.; Bourlinos, A. B.; Zbořil, R.; Otyepka, M. Cyanographene and Graphene Acid: Emerging Derivatives Enabling High-Yield and Selective Functionalization of Graphene. *ACS Nano* **2017**, *11* (3), 2982–2991.

(11) Mayo, D. W., Characteristic Frequencies of Aromatic Compounds (Group Frequencies of Arenes). In *Course Notes on the Interpretation of Infrared and Raman Spectra*, Mayo, D. W.; Miller, F. A.; Hannah, R. W., Eds., John Wiley & Sons, Inc., 2004; pp 101–140.

(12) Szabó, T.; Berkesi, O.; Forgó, P.; Josepovits, K.; Sanakis, Y.; Petridis, D.; Dékány, I. Evolution of Surface Functional Groups in a Series of Progressively Oxidized Graphite Oxides. *Chem. Mater.* **2006**, *18* (11), 2740–2749.

(13) Bourlinos, A. B.; Safarova, K.; Siskova, K.; Zbořil, R. The Production of Chemically Converted Graphenes from Graphite Fluoride. *Carbon* **2012**, *50* (3), 1425–1428.

(14) Sandford, G. Perfluoroalkanes. *Tetrahedron* **2003**, *59* (4), 437–454.

(15) Senthilnathan, J.; Weng, C.-C.; Liao, J.-D.; Yoshimura, M. Submerged Liquid Plasma for the Synthesis of Unconventional Nitrogen Polymers. *Sci. Rep.* **2013**, *3*, 2414.

(16) Zheng, Y.; Jiao, Y.; Zhu, Y.; Li, L. H.; Han, Y.; Chen, Y.; Du, A.; Jaroniec, M.; Qiao, S. Z. Hydrogen Evolution by a Metal-Free Electrocatalyst. *Nat. Commun.* **2014**, *5*, 3783.

(17) Singh, V.; Joung, D.; Zhai, L.; Das, S.; Khondaker, S. I.; Seal, S. Graphene Based Materials: Past, Present and Future. *Prog. Mater. Sci*. **2011**, *56* (8), 1178–1271.

(18) Terrones, H.; Lv, R.; Terrones, M.; Dresselhaus, M. S. The Role of Defects and Doping in 2D Graphene Sheets and 1D Nanoribbons. *Rep. Prog. Phys.* **2012**, *75* (6), 062501.

(19) Chronopoulos, D. D.; Bakandritsos, A.; Lazar, P.; Pykal, M.; Čépe, K.; Zbořil, R.; Otyepka, M. High-Yield Alkylation and Arylation of Graphene via Grignard Reaction with Fluorographene. *Chem. Mater.* **2017**, *29* (3), 926–930.

(20) Guérin, K.; Pinheiro, J. P.; Dubois, M.; Fawal, Z.; Masin, F.; Yazami, R.; Hamwi, A. Synthesis and Characterization of Highly Fluorinated Graphite Containing sp^2 and sp^3 Carbon. *Chem. Mater.* **2004**, *16* (9), 1786–1792.

(21) Wang, Y.; Lee, W. C.; Manga, K. K.; Ang, P. K.; Lu, J.; Liu, Y. P.; Lim, C. T.; Loh, K. P. Fluorinated Graphene for Promoting Neuro-Induction of Stem Cells. *Adv. Mater.* **2012**, *24* (31), 4285–4290.

(22) Karlický, F.; Datta, K. K. R.; Otyepka, M.; Zbořil, R. Halogenated Graphenes: Rapidly Growing Family of Graphene Derivatives. *ACS Nano* **2013**, *7* (8), 6434–6464.

(23) Mazánek, V.; Jankovský, O.; Luxa, J.; Sedmidubský, D.; Janoušek, Z.; Šembera, F.; Mikulics, M.; Sofer, Z. Tuning of Fluorine Content in Graphene: Towards Large-Scale Production of Stoichiometric Fluorographene. *Nanoscale* **2015**, *7* (32), 13646–13655.

(24) Nakajima, T.; Gupta, V.; Ohzawa, Y.; Groult, H.; Mazej, Z.; Žemva, B. Influence of Cointercalated HF on the Electrochemical Behavior of Highly Fluorinated Graphite. *J. Power Sources* **2004**, *137* (1), 80–87.

(25) Dubois, M.; Guérin, K.; Pinheiro, J. P.; Fawal, Z.; Masin, F.; Hamwi, A. NMR and EPR Studies of Room Temperature Highly Fluorinated Graphite Heat-Treated Under Fluorine Atmosphere. *Carbon* **2004**, *42* (10), 1931–1940.

(26) Sun, C.; Feng, Y.; Li, Y.; Qin, C.; Zhang, Q.; Feng, W. Solvothermally Exfoliated Fluorographene for High-Performance Lithium Primary Batteries. *Nanoscale* **2014**, *6* (5), 2634–2641.

(27) Coates, J., Interpretation of Infrared Spectra, A Practical Approach. In *Encyclopedia of Analytical Chemistry*, Meyers, R. A., Ed. John Wiley & Sons, Ltd., 2006.

(28) Niwano, M.; Takeda, Y.; Kurita, K.; Miyamoto, N. Hydrogen Termination of the NH_4F-Treated Si(111) Surface Studied by Photoemission and Surface Infrared Spectroscopy. *J. Appl. Phys.* **1992**, *72*, 2488–2491.

(29) Adamopoulou, T.; Papadaki, M. I.; Kounalakis, M.; Vazquez-Carreto, V.; Pineda-Solano, A.; Wang, Q.; Mannan, M. S. Thermal Decomposition of Hydroxylamine: Isoperibolic Calorimetric Measurements at Different Conditions. *J. Hazard. Mater.* **2013**, *254–255*, 382–389.

(30) Chronopoulos, D. D.; Bakandritsos, A.; Pykal, M.; Zbořil, R.; Otyepka, M. Chemistry, Properties, and Applications of Fluorographene. *Appl. Mater. Today* **2017**, *9*, 60–70.

(31) Wei, C.; Saraf, S. R.; Rogers, W. J.; Sam Mannan, M. Thermal Runaway Reaction Hazards and Mechanisms of Hydroxylamine with Acid/Base Contaminants. *Thermochim. Acta* **2004**, *421* (1–2), 1–9.

(32) Li, X.-F.; Lian, K.-Y.; Liu, L.; Wu, Y.; Qiu, Q.; Jiang, J.; Deng, M.; Luo, Y. Unraveling the Formation Mechanism of Graphitic Nitrogen-Doping in Thermally Treated Graphene with Ammonia. *Sci. Rep.* **2016**, *6*, 23495.

(33) Wang, B.; Tsetseris, L.; Pantelides, S. T. Introduction of Nitrogen with Controllable Configuration into Graphene *via* Vacancies and Edges. *J. Mater. Chem. A*. **2013**, *1* (47), 14927–14934.

(34) Bueno, R. A.; Martínez, J. I.; Luccas, R. F.; del Árbol, N. R.; Munuera, C.; Palacio, I.; Palomares, F. J.; Lauwaet, K.; Thakur, S.; Baranowski, J. M.; Strupinski, W.; López, M. F.; Mompean, F.; García-Hernández, M.; Martín-Gago, J. A. Highly Selective Covalent Organic Functionalization of Epitaxial Graphene. *Nat. Commun.* **2017**, *8*, 15306.

(35) Guo, D.; Shibuya, R.; Akiba, C.; Saji, S.; Kondo, T.; Nakamura, J. Active Sites of Nitrogen-Doped Carbon Materials for Oxygen Reduction Reaction Clarified Using Model Catalysts. *Science* **2016**, *351* (6271), 361–365.

(36) Telychko, M.; Mutombo, P.; Ondráček, M.; Hapala, P.; Bocquet, F. C.; Kolorenč, J.; Vondráček, M.; Jelínek, P.; Švec, M. Achieving High-Quality Single-Atom Nitrogen Doping of Graphene/SiC(0001) by Ion Implantation and Subsequent Thermal Stabilization. *ACS Nano* **2014**, *8* (7), 7318–7324.

(37) Wang, L.; Sofer, Z.; Luxa, J.; Pumera, M. Nitrogen Doped Graphene: Influence of Precursors and Conditions of the Synthesis. *J. Mater. Chem. C* **2014**, *2* (16), 2887–2893.

(38) Błoński, P.; Tuček, J.; Sofer, Z.; Mazánek, V.; Petr, M.; Pumera, M.; Otyepka, M.; Zbořil, R. Doping with Graphitic Nitrogen Triggers Ferromagnetism in Graphene. *J. Am. Chem. Soc.* **2017**, *139* (8), 3171–3180.

(39) Yun, S.-M.; Kim, J.-W.; Jung, M.-J.; Nho, Y.-C.; Kang, P.-H.; Lee, Y.-S. An XPS Study of Oxyfluorinated Multiwalled Carbon Nano Tubes. *Carbon Lett.* **2007**, *8* (4), 292–298.

(40) Greczynski, G.; Hultman, L. C1s Peak of Adventitious Carbon Aligns to the Vacuum Level: Dire Consequences for Material's Bonding Assignment by Photoelectron Spectroscopy. *ChemPhysChem* **2017**, *18* (12), 1507–1512.

(41) Williams, D. F.; Kellar, E. J. C.; Jesson, D. A.; Watts, J. F. Surface Analysis of 316 Stainless Steel Treated with Cold Atmospheric Plasma. *Appl. Surf. Sci.* **2017**, *403*, 240–247.

(42) Meyer, J. C.; Geim, A. K.; Katsnelson, M. I.; Novoselov, K. S.; Booth, T. J.; Roth, S. The Structure of Suspended Graphene Sheets. *Nature* **2007**, *446*, 60–63.

(43) Shao, Y.; Zhang, S.; Engelhard, M. H.; Li, G.; Shao, G.; Wang, Y.; Liu, J.; Aksay, I. A.; Lin, Y. Nitrogen-Doped Graphene and its Electrochemical Applications. *J. Mater. Chem.* **2010**, *20* (35), 7491–7496.

(44) Jeong, H. M.; Lee, J. W.; Shin, W. H.; Choi, Y. J.; Shin, H. J.; Kang, J. K.; Choi, J. W. Nitrogen-Doped Graphene for High-Performance Ultracapacitors and the Importance of Nitrogen-Doped Sites at Basal Planes. *Nano Lett.* **2011**, *11* (6), 2472–2477.

(45) Englert, J. M.; Dotzer, C.; Yang, G.; Schmid, M.; Papp, C.; Gottfried, J. M.; Steinrück, H.-P.; Spiecker, E.; Hauke, F.; Hirsch, A. Covalent Bulk Functionalization of Graphene. *Nat. Chem.* **2011**, *3*, 279–286.

(46) Guo, H.-L.; Wang, X.-F.; Qian, Q.-Y.; Wang, F.-B.; Xia, X.-H. A Green Approach to the Synthesis of Graphene Nanosheets. *ACS Nano* **2009**, *3* (9), 2653–2659.

(47) Nie, M.; Chalasani, D.; Abraham, D. P.; Chen, Y.; Bose, A.; Lucht, B. L. Lithium Ion Battery Graphite Solid Electrolyte Interphase Revealed by Microscopy and Spectroscopy. *J. Phys. Chem. C* **2013**, *117* (3), 1257–1267.

(48) Eigler, S.; Dotzer, C.; Hirsch, A.; Enzelberger, M.; Müller, P. Formation and Decomposition of CO_2 Intercalated Graphene Oxide. *Chem. Mater.* **2012**, *24* (7), 1276–1282.

(49) Szabó, T.; Berkesi, O.; Dékány, I. DRIFT Study of Deuterium-Exchanged Graphite Oxide. *Carbon* **2005**, *43* (15), 3186–3189.

(50) Eigler, S.; Hu, Y.; Ishii, Y.; Hirsch, A. Controlled Functionalization of Graphene Oxide with Sodium Azide. *Nanoscale* **2013**, *5* (24), 12136–12139.

(51) Zheng, Y.; Jiao, Y.; Ge, L.; Jaroniec, M.; Qiao, S. Z. Two-Step Boron and Nitrogen Doping in Graphene for Enhanced Synergistic Catalysis. *Angew. Chem. Int. Ed.* **2013**, *52* (11), 3110–3116.

(52) Biniak, S.; Szymański, G.; Siedlewski, J.; Świątkowski, A. The Characterization of Activated Carbons with Oxygen and Nitrogen Surface Groups. *Carbon* **1997**, *35* (12), 1799–1810.

(53) Zhang, J.; Zhao, Z.; Xia, Z.; Dai, L. A Metal-Free Bifunctional Electrocatalyst for Oxygen Reduction and Oxygen Evolution Reactions. *Nat. Nanotechnol*. **2015**, *10*, 444–452.

(54) Hellgren, N.; Haasch, R. T.; Schmidt, S.; Hultman, L.; Petrov, I. Interpretation of X-ray Photoelectron Spectra of Carbon-Nitride Thin Films: New Insights from *In Situ* XPS. *Carbon* 2016, **108**, 242–252.

(55) Scardamaglia, M.; Struzzi, C.; Osella, S.; Reckinger, N.; Colomer, J.-F.; Petaccia, L.; Snyders, R.; Beljonne, D.; Bittencourt, C. Tuning Nitrogen Species to Control the Charge Carrier Concentration in Highly Doped Graphene. *2D Mater.* **2016**, *3* (1), 011001.

(56) Bitter, J. H.; van Dommele, S.; de Jong, K. P. On the Virtue of Acid-Base Titrations for the Determination of Basic Sites in Nitrogen Doped Carbon Nanotubes. *Catal. Today* **2010**, *150* (1–2), 61–66.

(57) Kiuchi, H.; Shibuya, R.; Kondo, T.; Nakamura, J.; Niwa, H.; Miyawaki, J.; Kawai, M.; Oshima, M.; Harada, Y. Lewis Basicity of Nitrogen-Doped Graphite Observed by CO_2 Chemisorption. *Nanoscale Res. Lett.* **2016**, *11*, 127.

(58) Liu, S.; Wang, C.; Wei, Z.; Lv, W.; Fan, S.; Zhu, S.; Wang, F. One-Step Surface Modification of Multi-Walled Carbon Nanotubes by Pyrrole. *Mater. Lett.* **2014**, *134*, 91–94.

(59) Qian, T.; Yu, C.; Wu, S.; Shen, J. A Facilely Prepared Polypyrrole-Reduced Graphene Oxide Composite with a Crumpled Surface for High Performance Supercapacitor Electrodes. *J. Mater. Chem. A* **2013**, *1* (22), 6539–6542.